



HAL
open science

New insights into the ultrapotassic magmatism through xenoliths from the Eğirdir area, West Anatolia, Turkey

Platevoet Bernard, Bardintzeff Jacques-Marie, Elitok Ömer, Noret Aurélie,
Grégoire Michel, Poisson André

► To cite this version:

Platevoet Bernard, Bardintzeff Jacques-Marie, Elitok Ömer, Noret Aurélie, Grégoire Michel, et al..
New insights into the ultrapotassic magmatism through xenoliths from the Eğirdir area, West Anatolia,
Turkey. Arabian Journal of Geosciences, In press, 17 (1), pp.9. 10.1007/s12517-023-11766-7 . hal-
04337266

HAL Id: hal-04337266

<https://hal.science/hal-04337266>

Submitted on 12 Dec 2023

HAL is a multi-disciplinary open access archive for the deposit and dissemination of scientific research documents, whether they are published or not. The documents may come from teaching and research institutions in France or abroad, or from public or private research centers.

L'archive ouverte pluridisciplinaire **HAL**, est destinée au dépôt et à la diffusion de documents scientifiques de niveau recherche, publiés ou non, émanant des établissements d'enseignement et de recherche français ou étrangers, des laboratoires publics ou privés.



2 **New insights into the ultrapotassic magmatism through xenoliths**
3 **from the Eğirdir area, West Anatolia, Turkey**

4 Platevoet Bernard¹ · Bardintzeff Jacques-Marie¹ · Elitok Ömer² · Noret Aurélie¹ · Grégoire Michel³ · Poisson André¹

5 Received: 14 July 2023 / Accepted: 28 October 2023

6 © Saudi Society for Geosciences and Springer Nature Switzerland AG 2023

7 **Abstract**

AQ2 **AQ3** Plutonic xenoliths have been found within a pipe and a related phreatomagmatic leucitite deposit in the Eğırdir lake area, belonging to the Potassic-Ultrapotassic Afyon volcanic Province, West Anatolia. They consist of kamafugite-type, feldspar-bearing syenite, pyroxenite, leucitolite, some small-sized melilitolite and garnet-rich xenoliths, and a carbonatite. A new occurrence of kalsilite is described as either homogeneous acicular crystals or tabular two phases-exsolved crystals in the kamafugite-type and melilitolite xenoliths. Rock textures and compositions indicate cumulates and near-liquid composition rocks corresponding to relatively evolved magmas. All the rocks are strongly silica-undersaturated, Ca-, Mg-, and K-rich, and Al-poor. The fractional crystallization model includes clinopyroxene, apatite, phlogopite, melilite and leucite. Fe-Ti oxides and garnet may be also concerned. The P_{H_2O} during crystallization and differentiation is not more than 0.8 GPa. Major elements, trace elements, and REE patterns for xenoliths, which indicate near-liquid compositions, are typical of ultrapotassic series in a post-collisional geodynamic context, as it is the case for the Roman and Central ultrapotassic Italian provinces. The stable isotope ¹³C and ¹⁸O values of the calcio-carbonatite plot close to the primary carbonatite field, whereas the carbonates of the feldspar-bearing syenite and the peperite matrix suggest a low-T extensive contamination process. The origin of the carbonatite from kamafugite-type magmas by immiscibility or by fractional crystallization remains questionable; an origin by fractionation-melting of a metasomatized mantle source should be tested in the future.

AQ4 **Keywords** Ultrapotassic rock · Kamafugite · Leucitolite · Carbonatite · Turkey

A1 This work is dedicated to the late Dr. A. Poisson who have
A2 shown the studied area to the first author many years ago.

A3 Responsible Editor: Domenico M. Doronzo

A4 Bardintzeff Jacques-Marie
A5 jacques-marie.bardintzeff@universite-paris-saclay.fr

A6 Platevoet Bernard
A7 bernard.platevoet@orange.fr

A8 Elitok Ömer
A9 oelitok@gmail.com

A10 Noret Aurélie
A11 aurelie.noret@universite-paris-saclay.fr

A12 Grégoire Michel
A13 michel.gregoire@get.omp.eu

A14 ¹ UMR CNRS 8148 GEOPS, Université Paris-Saclay,
A15 Géosciences, GEOPS, Bât. 504, 91405 Orsay, France

A16 ² Department of Geological Engineering, Süleyman Demirel
A17 University, 32260 Isparta, Turkey

A18 ³ Géosciences Environnement, Toulouse, CNRS-CNES-IRD,
A19 Observatoire Midi-Pyrénées, 14 A. E. Belin, 31400 Toulouse,
A20 France

Introduction

23

**New occurrence of strongly silica-undersaturated,
potassic-ultrapotassic plutonic xenoliths**

AQ5

24
25

We report here the mineralogy and geochemical data for a new occurrence of melilite-, leucite-, kalsilite-bearing plutonic xenoliths found in the southern part of the Potassic-Ultrapotassic Afyon Province, Turkey. Some rare occurrences of such plutonic rocks have been previously found for example in the ejectas from Alban Hills and Montefiascone volcanism, Italy (Keller 1983; Peccerillo et al. 1984; Federico et al. 1994; Vollmer 1989; Beccaluva et al. 1991; Beccaluva et al. 2012; Peccerillo 1990, 1992, 1994; Di Battistini et al. 2001; Stoppa 2003; Stoppa et al. 2003a; Gaeta et al. 2006; Conticelli et al. 2013, 2015), and also in the ultrapotassic volcanic series from the East African rift (Bell and Powell 1969; Mitchell and Bell 1976; Pouclet 1980; Edgar and Arima 1981; Bergman 1987; Kampunzu and Lubala 1991; Laval and Hottin 1992; Bell and Tilton 2001; Stoppa

26
27
28
29
30
31
32
33
34
35
36
37
38
39
40

et al. 2003b). For a long time, authors have paid attention to the distinctive mineralogy of potassic-ultrapotassic rocks in relation with magma crystallization and differentiation (Yoder 1986; Veksler et al. 1998) and their complex hypothetical mantle source and successive mantle metasomatism events in relation with a post-collision, extensional geodynamical context (Savaşçin et al. 1994; Yağmurlu et al. 1997). However, there are few data regarding plutonic intracrustal intrusions especially for the tertiary Potassic-Ultrapotassic Afyon volcanic Province. Erosion processes did not allow access to the plutonic level, and only scarce mafic-ultramafic xenoliths entrained during volcanic events have been described and related to crustal intrusions (Akal 2003; Prelević et al. 2015).

Geological background

As part of the Alpine-Himalayan orogenic belt, Turkey consists of an amalgamation of Gondwana-derived continental blocks associated with ophiolitic units. The Anatolide-Tauride block which occupies western and southern parts of Turkey is subdivided into zones based on the type of metamorphism and age of deformation (Fig. 1a, b): Tavşanlı Zone, Afyon Zone, Menderes Massif, Bornova Flysch Zone, and Tauride Belt. The first four zones are characterized by medium-high-pressure metamorphic rocks (Bornova Flysch Zone). These zones are the low-grade metamorphic basement intruded by felsic igneous rocks (Tauride Belt, Gürsu et al. 2004), Mesozoic to Cenozoic sedimentary sequences, and stack of imbricated, ophiolite-bearing allochthonous nappes. The western part of the Tauride carbonate axis forms a north-pointing cusp in the north of Eğirdir Lake, the so-called Isparta Angle, and includes the study area. The northeast-southwest trending Beydağları platform carbonate separates allochthonous ophiolitic rock units with, from west to east, the Lycian nappes, the Antalya complex, and the Hoyran-Beyşehir-Hadım nappes. These four nappe systems join around Eğirdir Lake (Fig. 1b). Southwestern Turkey has been subjected to compressional and extensional tectonic activities, ophiolite emplacements, block rotations, and volcanic activities throughout Phanerozoic time.

Neotectonic structures developed in SW Turkey during the Late Miocene to Early Pliocene with local effects at the end of Middle Oligocene in a transtensional regime (Koçyiğit 1984a, b). They correspond to regional uplift, continental sedimentation (thick pile of molasse deposition), syn-sedimentary volcanism, and block faulting.

Potassic-ultrapotassic volcanisms in West Anatolia

North-south trending volcanic rocks, named Kırka-Afyon-Isparta Volcanic Province (Francalanci et al. 2000) or Kırka-Afyon-Isparta Alkaline Volcanic assemblage (after Savaşçin

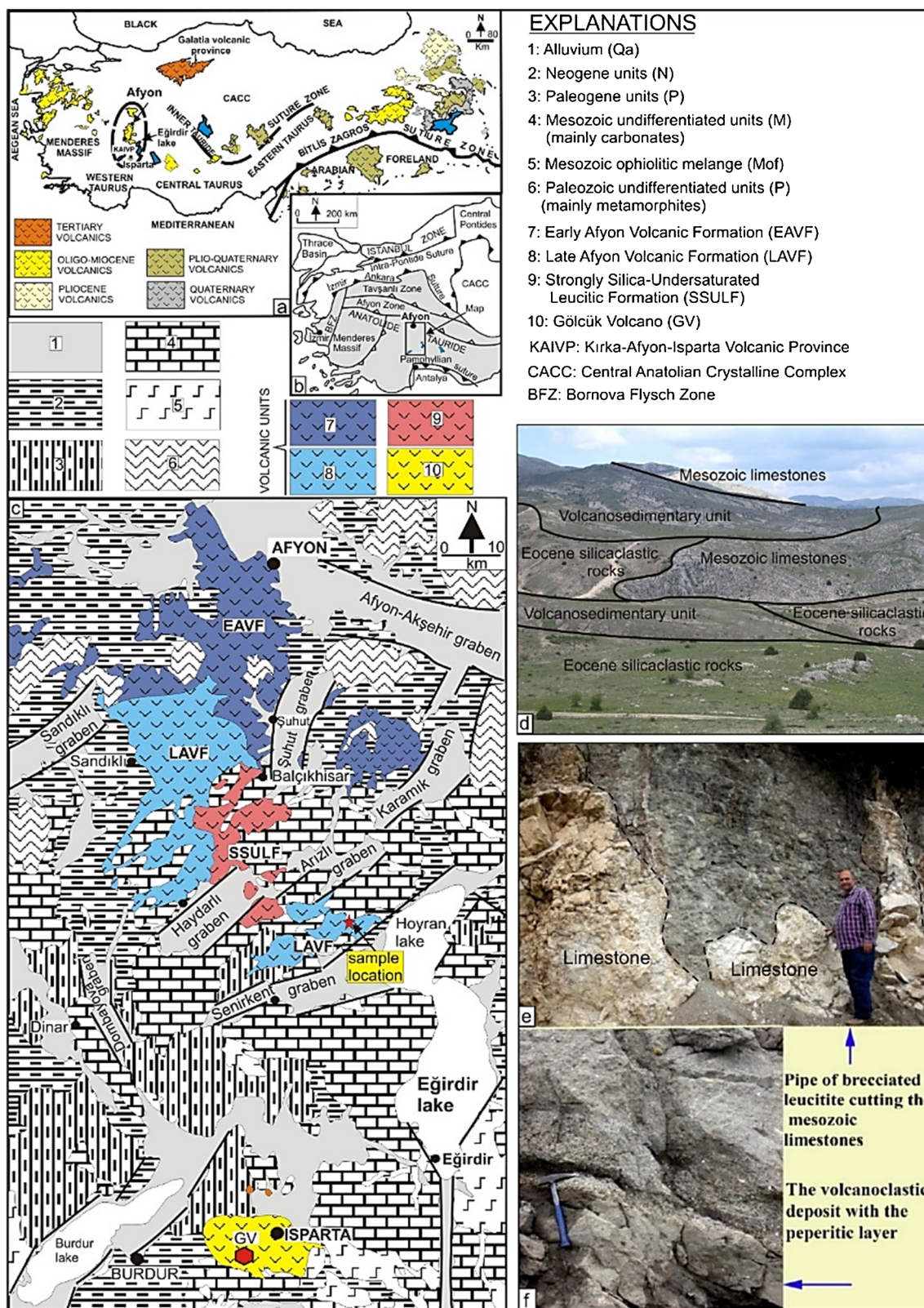
and Oyman 1998), crop out from the apex of the Isparta Angle to the north of Afyon, including the studied area, and are characterized mainly by potassic-ultrapotassic volcanic rocks (Fig. 1a, c) (Alici et al. 1998; Francalanci et al. 2000; Akal 2003; Platevoet et al. 2008, 2014; Elitok 2019; Prelević et al. 2012, 2015; Akal et al. 2013). In general, from north to south in the Kırka-Afyon-Isparta volcanic Province, volcanic activities get younger: 14.8 and 8.6 Ma around Kırka-Afyon (Francalanci et al. 2000) in the north, from 4.7 ± 0.2 Ma around Isparta (Lefèvre et al. 1983) to 24 ± 2 ka (Platevoet et al. 2014) and 12.9 ± 0.4 ka (Schmitt et al. 2014; Guillou et al. 2017) in the south, corresponding to the last volcanic events of the Gölcük volcano. The volcanic activities in SW Turkey are in close relationship with the neotectonic evolution of the region.

The Tertiary-Quaternary volcanic Province of West Anatolia is divided into a northern series named the Potassic-Ultrapotassic Afyon volcanic Province (Akal 2003; Akal et al. 2013; Prelević et al. 2012, 2015) extending north to south, from Afyon to Eğirdir Lake (Fig. 1b). It is formed by three main series, including a strongly silica-undersaturated, leucite-bearing volcanic series located at the southern part where we found the xenoliths, the subject of the present study. The Isparta potassic volcanic series is more recent, with the Quaternary Gölcük volcano situated in the so-called Isparta Angle (Lefèvre et al. 1983; Alici et al. 1998; Platevoet et al. 2014, 2015; Çoban et al. 2019).

Field occurrence

Sample locations are in the NW Hoyran lake (N Eğirdir lake), within a NE-SW trending horst structure bounded by the Senirkent graben in the south (Fig. 1c) and the Haydarli graben in the north. Mesozoic formations consisting mainly of massive or bedded limestones form the basement (Fig. 1c, d), locally unconformably overlain by Eocene flysch-type deposit, or by Upper Miocene-Pliocene volcano-sedimentary deposits (Elitok 2019, and references therein). Trachytic domes are observed in the west of the studied area and leucite-bearing lava dome flows are observed to the NW close to the Haydarli graben.

Along the Afyon-Karahisar road, the Cretaceous limestones and Cenozoic lacustrine levels are cut by a volcanic pipe 5 m wide (Fig. 1e). This pipe consists of a leucite-bearing brownish volcanic material including numerous xenoliths of volcanic and plutonic types. At the contact between the pipe and the limestone basement, the limestones are brecciated and some blocks are incorporated in the volcanoclastic breccia. The xenoliths and the enclosing matrix are extensively hydrothermally altered by a CO₂-dominant fluid phase, as evidenced by millimeter- to centimeter-size calcite veins.



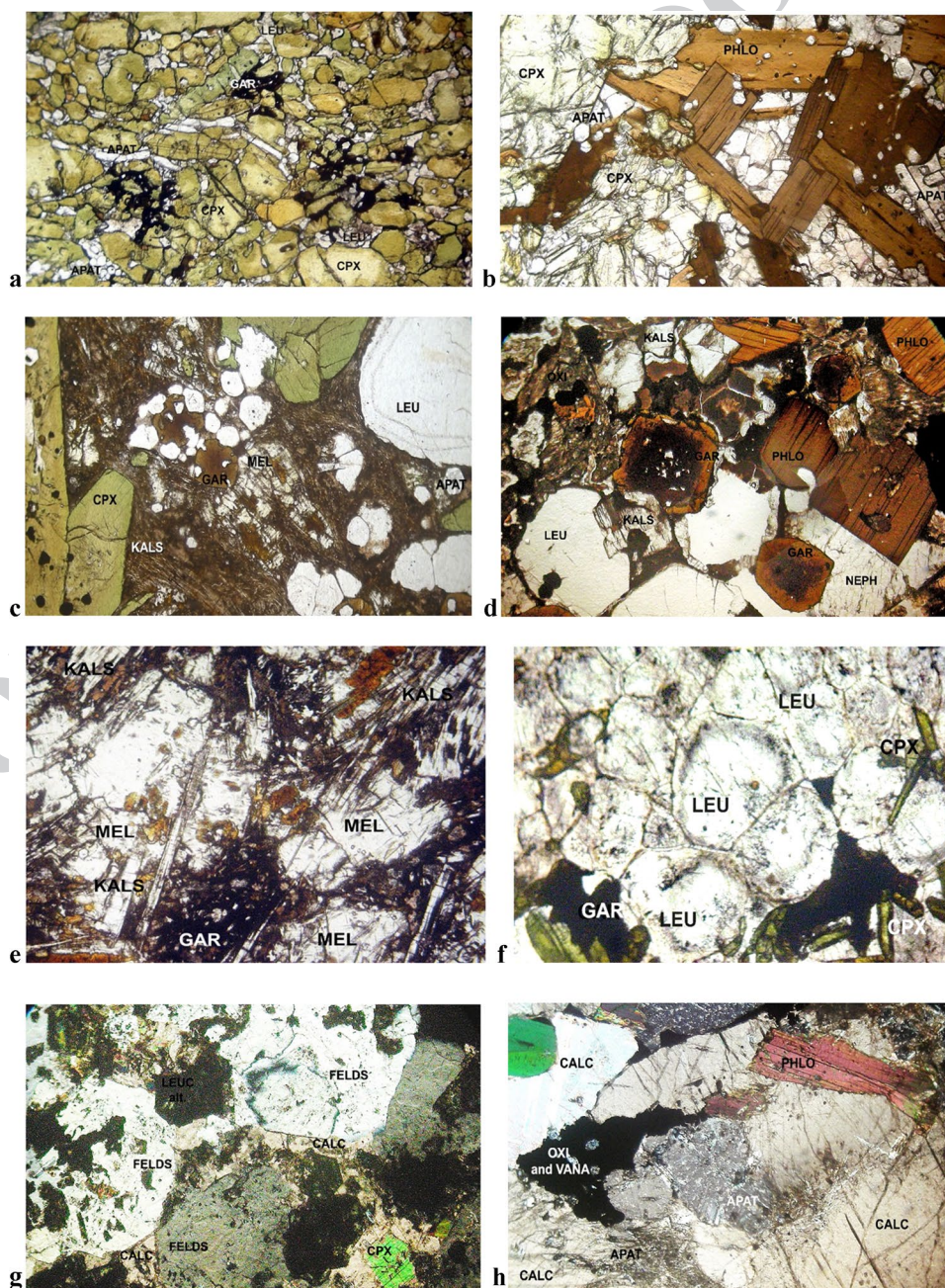
AQ6 Fig. 1 Geographic situation and geological map. Localization of the studied area and geological map from Isparta to Afyon northwest of Eğirdir Lake, Anatolia; a volcanics in Anatolia; b structural scheme of West Anatolia; c main geological units from Afyon to Isparta; d

local geological units near the studied area; e top, the leucitite pipe with limestone blocks and xenoliths; f the volcanoclastic deposit, the peperite has a white calcitic matrix including black leucitite granules

140 Near the pipe, towards the south, a volcanoclastic deposit
 141 is formed by a brecciated leucitite, which also contains
 142 numerous xenoliths. The lower part of this volcanoclastic
 143 deposit is composed of a 50-cm-thick layer of a pulverized
 144 leucitite lava in a calcitic-zeolitic matrix, similar to a pep-
 145 erite (Fig. 1e, f). The xenoliths (5 to 20 cm in size)
 146 were collected in this volcanoclastic deposit. They are angular
 147 or rounded and show a variety of textures from fine-grained
 148 porphyric textures to equant coarse-grained textures (Fig. 2).

The xenoliths are leucocratic to melanocratic, depending
 on their mafic-felsic mineral assemblage. Small ultramafic
 xenoliths (no more than 5 cm in size) and a single coarse-
 grained carbonatite xenolith (10 cm in size) were also found.
 The xenoliths are relatively well preserved from hydrother-
 mal alteration and provide a good opportunity for a petro-
 logical study in order to specify their possible connection
 with the Potassic Ultrapotassic Afyon volcanic Province.

Fig. 2 Rock textures: **a** pyroxenite with clinopyroxene, apatite, and garnet; **b** pyroxenite with clinopyroxene, apatite, and phlogopite; **c** microgranular texture of kamafugite with clinopyroxene, apatite, leucite, melilite, and kalsilite; **d** coarse-grained texture of kamafugite with clinopyroxene, apatite, leucite, garnet, kalsilite, and phlogopite; **e** melilitite with melilite, apatite, kalsilite, and garnet; **f** leucitilite with leucite, clinopyroxene, garnet (coarse-grained texture); **g** feldspar-bearing syenite with clinopyroxene, ghost of leucite, alkali feldspar, and calcite; **h** carbonatite with calcite, apatite, phlogopite, Fe-oxide, and vanadinite



157 Analytical methods

158 Mineral compositions were determined at CAMPARIS
 159 Lab. (Université Paris-Sorbonne, France), using the
 160 Cameca SX 100 or Cameca SX Five electron probe
 161 microanalyzers (with 4 or 5 wavelength-dispersive spec-
 162 trometers). Element calibrations were done using a set of
 163 silicates, oxides, and REE-doped glasses. Accelerating
 164 voltage and beam current were $U = 15$ kV, $I = 10$ nA, with
 165 a beam of 1–5 μm wide; the counting times for each ele-
 166 ment were 10 s and 5 s for background on each side of
 167 the measured X-ray peak for each element. The mineral
 168 compositions are calculated using a Z.A.F. iterative matrix
 169 correction. Mineral structural formulae were calculated on
 170 a classical stoichiometric basis chosen for each mineral
 171 species.

172 ^{18}O and ^{13}C stable isotope analyses were carried out
 173 on calcite extracted from magmatic rocks and the lime-
 174 stone basement. Calcite powder was reacted with 100%
 175 orthophosphoric acid at 25 °C and the derived CO_2 was
 176 analyzed using a VG Sira 10 mass spectrometer to deter-
 177 mine O and C isotope composition at the GEOPS labora-
 178 tory (Université Paris-Saclay, France). All isotopic values
 179 are reported in the standard δ -notation in per mil relative
 180 to V-PDB (Vienna Pee Dee Belemnite) by assigning a $\delta^{13}\text{C}$
 181 value of +1.95‰ and a $\delta^{18}\text{O}$ value of –2.20‰ to NBS19.
 182 Reproducibility was checked by a replicate analysis of
 183 laboratory standards and was $\pm 0.1\%$ for carbon isotopes
 184 and $\pm 0.2\%$ for oxygen isotopes.

185 Whole-rock major and trace element concentrations
 186 of the samples were determined by inductively coupled
 187 plasma optical emission spectrometry and inductively cou-
 188 pled plasma mass spectrometry, respectively at the Service
 189 d'Analyse des Roches et des Minéraux (SARM, CRPG,
 190 Nancy, France). CO_2 analyses of the fire loss on ignition
 191 were carried out for each rock.

192 The volcanoclastic deposit: leucite 193 and peperite

194 The volcanoclastic deposit consists of a brecciated and
 195 hydrothermally altered leucite (Fig. 1e). At the base of
 196 the deposit, there is a 50-cm-thick layer of a mixture of
 197 dark leucite granules enclosed in a white matrix com-
 198 posed essentially of calcite and zeolites. This 50-cm-thick
 199 layer seems to be a peperite (Fig. 1f). Similar deposits are
 200 commonly described during explosive phreatomagmatic
 201 eruptive events occurring within lacustrine areas. The
 202 gray-black leucite granules contain phenocrysts of clino-
 203 pyroxene and leucite in an essentially dark microlithic

groundmass composed of opaque oxide, feldspar, clino-
 pyroxene, apatite, and glass. The granules are surrounded
 by a matrix composed of calcite and zeolites. Some clino-
 pyroxenes are isolated during the granulation process of
 leucite. The volcanoclastic deposit also contains some
 well-preserved angular to more rounded enclaves of leuci-
 tite, very similar in texture and mineral paragenesis to the
 leucite matrix of the volcanoclastic deposit.

Main petrological groups of xenoliths

Forty xenoliths were investigated and divided into five
 groups (Table 1), according to their mineral paragenesis
 (Table 1): pyroxenites, plutonic kamafugite-type rocks, leu-
 citolites, syenites, and only one carbonatite xenolith.

The pyroxenite xenoliths

Pyroxenites (Fig. 2a, b; Table 1) are ultramafic rocks with
 more than 90 vol.% of mafic minerals (clinopyroxene, phlo-
 gopite) associated with numerous prismatic crystals of apa-
 tite and minor amounts of interstitial felsic minerals (<10
 vol.%). Phlogopite, when present (0–20 vol. %), is typically
 subhedral to anhedral, crystallizing after clinopyroxene
 and apatite (Fig. 2b). Dark interstitial melanite-type garnet,
 leucite, zeolites, and calcite are present in small amounts.
 Leucite is commonly replaced by a mixture of zeolite, cal-
 cite, and phyllosilicate. These xenoliths are very similar to
 ultramafic xenoliths from the Potassic Ultrapotassic Afyon
 volcanic Province described by Prelević et al. (2015).

The kamafugite-type xenoliths

These xenoliths contain from 5 to 30 vol.% of kalsilite
 (KAlSiO_4), 25–30 vol.% of leucite, nepheline, and no
 feldspar. Kalsilite has never been described before in the
 previous studies of the Potassic-Ultrapotassic Afyon vol-
 canic Province (Akal et al. 2013; Prelević et al. 2015; Elitok
 2019). It also occurs in the Western Africa Rift ultrapotassic
 magmatism and in the Italian Roman Province (Di Battistini
 et al. 2001; Tappe et al. 2003; Stoppa et al. 2003a). Two
 main textures of kamafugite-type xenolith are observed:
 a microgranular porphyritic texture and a coarse-grained
 texture.

The microgranular porphyritic xenoliths have variable
 modal compositions (Fig. 2c, Table 1) with porphyrocrysts
 of leucite, zoned clinopyroxene including tiny early Ti-
 magnetite, prismatic melilite, and later idiomorphic zoned
 (black core to yellow rim) garnet and magnetite. Kalsilite is
 typically the last major mineral to crystallize in these rocks,
 after apatite, clinopyroxene, magnetite, melilite, and just
 before garnet. Garnet includes other phases like melilite,

Table 1 Modal composition of studied plutonic xenoliths and leucitite

Rock Nb	98-A Melilitolite	98,004	98,006	98,005	98,008	E-17 Carbonatite	E8	E9 Pyroxenite group	E12
Leucite		30	30	25	25		5	5	+
Melilite	45		10	15	7				
Kalsilite	30	5	15	25	15				
Nepheline		18	5		20				
Altered foide		5	10		5				
Feldspath					+				
Clinopyroxene				20	15		80	60	75
Garnet	20	15	10	10			5		
Calcite		3	10		3	90		2	5
Apatite	2	2	3		+	5	8	7	7
Mica		18			10	2		25	
Titanomagnetite		+		5	+	2			
Others (zeolites)	3	+	5		+	1	2	1	12
Groundmass									
Rock Nb	E11 Leucititolite group	E3	E4	E5	E6	E7	E10 Syenite	E2 Leucitite	
Leucite	70	45	65	70	60	60	10	30	
Melilite									
Kalsilite		3				3			
Nepheline									
Altered foide	5	7			10	10	5	+	
Feldspath			3				65	+	
Clinopyroxene	10	35	20	10		5	5	20	
Garnet	10		10	15	12	10			
Calcite					5		10		
Apatite		5	2	2	2	3	2	+	
Mica	5		2	2	5		2		
Titanomagnetite								+	
Others (zeolites)		3					1	+	
Groundmass								50	

apatite, and thin elongate prisms of kalsilite, attesting of its late nucleation and growth. Kalsilite exhibit clusters of very elongated homogeneous prisms forming the micro-granular groundmass of the rock (Fig. 2c).

The coarse-grained xenoliths (Fig. 2d, e) not only have the same mineralogy, with apatite, leucite, prismatic kalsilite, and zoned garnet but they also contain phlogopite. Clinopyroxene is less abundant and melilite is rare or absent. In coarse-grained xenoliths, kalsilite and nepheline crystallize as separate phases. Kalsilite forms euhedral, tabular crystals (Fig. 2d) showing kalsilite-nepheline exsolution intergrowths (Fig. 3), symptomatic of subsolidus reequilibration. Such exsolution intergrowths have been described in Mt Nyiragongo lava (Congo), in melilitolites, kalsilitites, and kamafugites from Roman Province and Intramountain Ultra-alkaline Province, Italy (Aurisicchio and Federico 1985; Federico et al. 1994, Stoppa and

Woolley 1997; Stoppa et al. 2003a). Melilite is associated with variable amounts of clinopyroxene, garnet, apatite, phlogopite, Ti-magnetite, and calcite, while olivine is not present. Calcite and brown-yellowish phases (a mixt of hydroxide amorphous phases and phyllosilicates) commonly replace the core of melilite crystals. Intergrowth features between garnet and leucite are common. Large crystals of nepheline can be relatively abundant (5 to 20 vol.%) in these xenoliths and calcite is interstitial. Two small (no more than 5 cm in size) mafic-ultramafic xenoliths also belong to this group. The first xenolith is extremely rich in melilite (45 vol.%, Table 1 sample 98-A), and can be named melilitolite. The second xenolith is a garnet-rich type; a similar garnet-bearing xenolith has been also described in the leucitites from the Balçıkhisar volcanic area (Akal et al. 2013).

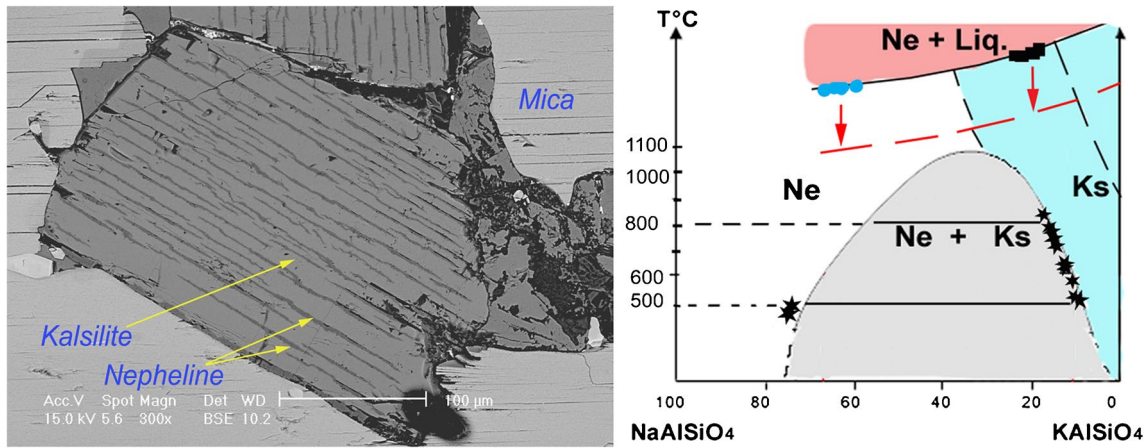


Fig. 3 Kalsilite and nepheline compositions. Microprobe back-scattered picture of euhedral kalsilite, crystal showing exsolution features: fine exsolution lamellas of nepheline. Nepheline-kalsilite versus T°C diagram showing the position of kalsilite analyses in relation with solidus and solvus curves; the red curve is a more realistic

solidus position relative to temperature for the hypersolvus kalsilite. The blue line would be the solidus-solvus intersection given by the compositions of separate crystals of nepheline and exsolved kalsilite found in coarse-grained kamafugite-type xenolith (after Tuttle and Smith 1958; Zeng and MacKenzie 1984)

283 **The leucitolite xenoliths**

284 Leucitolites are the commonest and largest plutonic xeno-
 285 liths (10–15 cm in size). They are mostly coarse-grained
 286 and their mineral parageneses differ only in the relative
 287 mafic to felsic mineral ratio, in particular leucite, varying
 288 from 45 to 70 vol.%, and giving mesocratic to leucocratic
 289 type rocks (Fig. 2f). Adjacent crystals of leucite typically
 290 show 180° triple joins, suggesting leucite crystal segrega-
 291 tion, followed by textural subsolidus re-equilibration and
 292 crystal aging (Boudreau 1995; Marsh 1998, 2007; Laporte
 293 and Provost 2000; McBirney 2007; McBirney et al. 2009).
 294 This process of subsolidus re-equilibration can happen dur-
 295 ing slow cooling of magmatic intrusions, but it remains
 296 controversial in particular for felsic intrusions (Holness and
 297 Vernon 2014; Holness et al. 2017, 2018). Leucite is locally
 298 partially replaced by a mixture of alkali feldspar and zeolite.
 299 The other mineral phases are euhedral green clinopyroxene,
 300 prismatic apatite, poikilitic garnet, Ti-Fe oxides, and phlo-
 301 gopite. Kalsilite is rare in leucitolite and occurs as poikilitic,
 302 commonly altered crystals located between euhedral leucite
 303 crystals. Textural features such as two-phase layering, with
 304 pyroxene-rich thin layers and extremely rich leucite layers,
 305 are symptomatic of crystal segregation by a rheological pro-
 306 cess or by a density-driven cumulative process within the
 307 magma intrusions.

308 **Feldspar- and leucite-bearing syenite xenoliths**

309 Their textures are fine-grained to coarse-grained (Fig. 2g). As
 310 for kamafugite-types and leucitolites, the mineral paragenesis
 311 consists of not only euhedral zoned (green core to dark green
 312 rim) clinopyroxene, prismatic apatite, and euhedral leucite

but also rare euhedral kalsilite prism in some xenoliths, and
 sometimes nepheline. Zoned garnet and poikilitic zoned alkali
 feldspar are observed. Few sections of pale-brown mica and
 Ti-Fe oxides are observed. The paragenesis variations from
 one sample to one another are dependent upon the destabili-
 zation degree of leucite which is partially or totally replaced
 by large, poikilitic feldspars. Calcite also crystallized as a pri-
 mary phase in some feldspar-bearing syenite, in relation to a
 CO₂-enriched dissolved fluid phase.

The carbonatite xenolith

A single 10-cm-sized xenolith of carbonatite has been found,
 representing the first occurrence of coarse-grained carbonatite
 in this area. It consists of large crystals of calcite with clusters
 of prismatic apatite. Frequent pale-brown phlogopite exhib-
 its sector zoned subhedral crystals. Magnetite and vanadinite
 have crystallized lately and are interstitial between calcite and
 apatite crystals (Fig. 2h).

At the apex of the so-called Isparta Angle, from the Senir-
 kent area (Elitok 2019), inclusions and microscopic blobs of
 carbonatite have been also observed in a leucite-bearing pho-
 nolite. These small blobs and inclusions are mainly formed by
 carbonate with various amounts of phlogopite, clinopyroxene,
 leucite or nepheline, apatite, and garnet (Elitok 2019).

Mineral composition results

Leucite

Leucite compositions (Appendix 1A) are usually near the
 ideal formulae with very small amounts of Na₂O, FeO, and

340 BaO (<0.8 wt.%). The leucite of pyroxenite and syenite
 341 has undergone hydration. It has been partially replaced by
 342 a mixture of feldspar, calcic zeolite, and calcite (see altered
 343 leucite in Appendix 1A). Replacement of leucite by analcite
 344 is not observed, probably due to very low sodium content.
 345 The main feature that occurs in some syenite xenoliths is the
 346 partial or almost total disappearance of leucite, replaced by
 347 alkali feldspar and nepheline, corresponding to the subsoli-
 348 dus breakdown of leucite in the presence of water (Fudali
 349 1963).

350 **Kalsilite and nepheline**

351 Homogeneous thin elongate prisms of kalsilite (Fig. 3;
 352 Appendix 1B) are relatively Na₂O-rich with a maximum
 353 of 21 mol% of nepheline, corresponding to the preserved
 354 hypersolvus composition of kalsilite during rapid cooling.
 355 Based on the experimental study of Tuttle and Smith (1958),
 356 the crystallization temperature would be ≥ 1000 °C (Fig. 3).

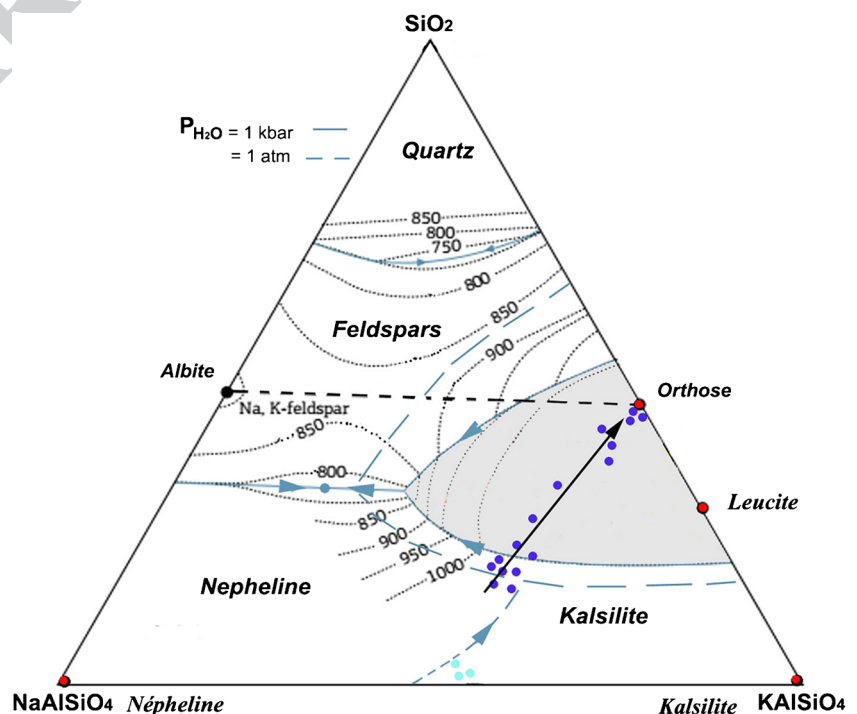
357 The kalsilite of the coarse-grained kamafugite-type con-
 358 tains 7–11 mol% of nepheline component, and the exsolved
 359 nepheline lamellae have 25–26 mol% of kalsilite component,
 360 indicating a solvus exsolution process during slow cool-
 361 ing, operating between 800 and 500 °C. In coarse-grained
 362 kamafugite and feldspar-bearing syenite, crystals of nephe-
 363 line rim leucite form large anhedral crystals showing some
 364 cancrinite-type alteration. Compared to the nepheline exso-
 365 lution lamellae from the exsolved kalsilite crystals, these
 366 nepheline crystals are relatively potassic, with 35–39 mol%
 367 of kalsilite component. This compositional range (Fig. 3) is

368 consistent with the subsolvus kalsilite-nepheline pairs crys-
 369 tallizing as separate crystals, at about 800 °C under 0.5 GPa,
 370 according to the experimental study of Zeng and MacKenzie
 371 (1984), whereas the solvus exsolution process of kalsilite
 372 has operated between 800 and 500 °C during slow cooling
 373 (Fig. 3).

374 **Alkali feldspar**

375 The first feldspar to crystallize in syenite belongs to the hyal-
 376 ophane type (Appendix 1C). Crystals are strongly zoned; the
 377 Ba-rich core has 12–13 wt.% BaO, giving 25 mol% of cel-
 378 sian component, and subsequent decrease of K₂O and Na₂O
 379 wt.%. SrO reaches a maximum of 2.5 wt.% corresponding to
 380 6 mol.% of the stromalolite component Na₂SrAl₄Si₄O₁₆ (see
 381 Essene et al 2005). Crystal rims evolve to pure K-feldspar.
 382 The feldspar of the leucite lava is also Ba-rich (25 mol% of
 383 celsian component) and is more Ca- and Sr-rich than those
 384 of the syenite. This Ba-feldspar is plotted in the quartz-
 385 nepheline-kalsilite ternary system (Fig. 4). Ba, equivalent
 386 of K and Na, is allocated to the calculated nepheline and
 387 kalsilite components. The hyalophane feldspar plots in the
 388 feldspathoid-bearing area of that diagram, due to Ba enrich-
 389 ment and coupled Si-Al substitution. When leucite was
 390 replaced during the crystallization of silica-undersaturated,
 391 Ba-rich, K-rich, and Na-poor magma, hyalophane feldspar
 392 crystallized in place of kalsilite or nepheline, which are both
 393 unable to incorporate large amounts of Ba and Sr in their
 394 structures. In the Qz-Ne-Ks diagram, hyalophane feldspar
 395 plays the same role as feldspathoid because of its strong

Fig. 4 Hyalophane and K-feldspar in the system nepheline-kalsilite-quartz ternary diagram. Considering that Sr and Ba are equivalent to Na and K with equal repartition between the two poles. Blue dots: present study; pale-blue dots: analyses from Akal (2003)



396 silica deficiency compared to typical K-feldspar. The E10
 397 feldspar-bearing syenite (Table 2) illustrates this well: the
 398 rock is strongly silica-deficient, Ba- and Sr-rich (11,000 ppm
 399 of Ba, 2250 ppm of Sr), and Na-poor (0.25w.% Na₂O). Leu-
 400 cite was destabilized and was first replaced by hyalophane
 401 feldspar instead of kalsilite or/and nepheline, followed by
 402 K-feldspar crystallization. The control by Sr and Ba on feld-
 403 spar crystallization has been previously pointed out by Fer-
 404 guson and Cundari (1982) in leucite-bearing magmas. Ba
 405 and Sr elements are important substitutes for K, Na, and Ca,
 406 particularly in potassic-ultrapotassic silica-undersaturated
 407 magmatism (Cundari 1979; Mitchell and Vladikin 1996;
 408 Akal 2003; Platevoet et al. 2014; Caran 2016). To the best
 409 of our knowledge, there seems to be no experimental system
 410 that investigates the effect of Ba and Sr on the stability of
 411 feldspar-feldspathoid phases in the Qz-Ne-Ks ternary sys-
 412 tem, and also in the more complex Qz-Ne-Ks-An quater-
 413 nary system (Carmichael et al. 1974). These systems would
 414 probably show major changes if Ba and Sr elements were
 415 considered instead of Na, in a K-rich, highly silica-deficient
 416 experimental system.

417 Clinopyroxene

418 The composition of clinopyroxene (Appendix 1D) evolves
 419 from diopside to augite and from augite to aegirine-augite
 420 in the most evolved rocks. CaO and MgO contents are high,
 421 especially in crystal cores of ultramafic and mafic xenoliths
 422 (Fig. 5), but decrease from kamafugite-type to leucitolite,
 423 syenite xenolith, and in leucitite lava. CaO and MgO con-
 424 tents decrease in the crystal rims together with SiO₂, while
 425 FeO_t, Al₂O₃ (< 4.60 wt.%), and TiO₂ (< 1.4 wt.%) contents
 426 increase, probably due to the decrease of silica activity dur-
 427 ing the crystallization. The aegirine component rises in the
 428 more evolved syenite xenoliths and in leucitite, a common
 429 feature of the silica-undersaturated series evolving under
 430 relative oxidizing conditions, and/or due to the alkali-ferric
 431 effect in peralkaline magmas (Larsen 1976; Mitchell and
 432 Platt 1978, 1982; Mitchell and Vladykin 1996). Tschermak
 433 molecules, especially Fe-Tschermak mol., rise from core to
 434 rim of crystals and from the less evolved ultramafic-mafic
 435 groups (pyroxenite and kamafugite) to the more felsic
 436 groups (leucitolite and syenite) and leucitite. In the Ti vs.
 437 Al_I diagram (Fig. 5), the majority of clinopyroxene analy-
 438 ses plot in the transitional field and the HKS-KS field of
 439 Perini and Conticelli (2002) and in the kamafugite field for
 440 pyroxene depicted by Prelević et al. (2005, 2015). However,
 441 some analyses of the kamafugite xenoliths are very poor in
 442 TiO₂. This can be due to early crystallization of both Ti-
 443 magnetite and clinopyroxene (rock 98005, Fig. 2c), Ti being
 444 prior incorporated in Ti-magnetite under relative elevated
 445 fO₂. The clinopyroxene of melilite leucitite from Meşebaşı
 446 described by Akal (2003) belongs to the lamproite field of

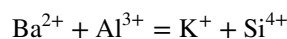
Mitchell and Bergman (1991) and differs from clinopyrox-
 ene of the Eğırdir leucitite lava.

Melilite

447
 448
 449
 450 Compositions of melilite (Appendix 1E) are plotted in the
 451 Na-melilite/gehlenite/akermanite ternary system (Fig. 6).
 452 They are poor in gehlenite and rich in akermanite compo-
 453 nents. They are relatively similar in composition to melilite
 454 from Montefiascone pyroxenites of the Roman Province
 455 and San Venanzo melilitolite (Stoppa et al. 2003a), but
 456 they are lower in gehlenite than the melilites of the Alban
 457 Hills ejecta (Stoppa et al. 2003a). Finally, they are more
 458 Mg-rich, and Al- and Na-poor compared to the melilite of
 459 the northern Meşebaşı melilite-bearing leucitites from the
 460 northern Potassic-Ultrapotassic Afyon volcanic Province
 461 (Akal 2003).

Phlogopite

462
 463 All mica can be classified as phlogopite (Appendix 1F) with
 464 a Mg/Mg + Fe + Mn ratio ranging from 0.90 to 0.60. Their
 465 Ti content is highly variable, being generally > 2.5 wt.% in
 466 pyroxenite and decreasing through kamafugite and leuci-
 467 tolite groups, and is very low in phlogopite from syenite
 468 and carbonatite xenoliths. F content is low to moderate in
 469 pyroxenite, leucitolite, and kamafugite-type (from 0.3 to
 470 1.13 cation pfu.), but more elevated in the feldspar-bear-
 471 ing syenite with 1.2 to 2.6 cations pfu., probably in rela-
 472 tion with a [F + CO₂]-rich, H₂O-poor dissolved fluid phase.
 473 BaO in phlogopite is high and increases from pyroxenite to
 474 kamafugite and leucitolite, from around 1.0 up to 6.1 wt.%.
 475 The main coupled substitution that governs Ba incorpora-
 476 tion involves Si, Al, and Ti, also Fe and Mg, in place of
 477 Ti and K in the interlayer site (Wagner and Velde 1986;
 478 Wagner et al. 1987; Edgar 1992; Seifert and Kämpf 1994).
 479 The most barium-rich phlogopite occurs in the carbonatite
 480 xenolith with a maximum of 13 wt.% BaO. The crystals
 481 show obvious sector zoning (Fig. 7A) due to strong Ba vari-
 482 ations associated with coupled Al, Si, and K substitutions.
 483 The correlation (Fig. 7B) observed between [Ba + Al_{IV}] and
 484 [Si + K] pointed out the main substitution:



486
 487 Ba-rich phlogopite is frequent in potassic-ultrapotassic
 488 magmatism. Such high BaO values, between 13 and 16
 489 wt.%, have been observed in phlogopite (Fig. 7C) from the
 490 Jacupiranga carbonatite, Brazil (Gaspar and Wyllie 1982),
 491 and also in phlogopite of numerous nephelinites, ankara-
 492 trites, and kamafugites from various localities (Mansker
 493 et al. 1979; Gaspar and Wyllie 1982; Edgar 1992; Seifer
 494 and Kämpf 1994; Stoppa et al. 2003c; Prelević et al.

Table 2 Major and trace elements whole-rock analyses, and calculated CIPW norm

Whole-rock analysis	Kamafu-gite-type rocks		Syenite	Leucitites		Pyroxenites		Leucitites				Carbonatite				
	Mellitite	Kalsilite rock	Kalsilite rock	E10	E2	E1*	Phlo. Leuc	E12	E8	E3	E4	E7	E5	E11	E6	E17
rock Nb	98,005	98-004	98-008	44.59	49.89	43.65	41.35	42.06	45.24	48.04	45.14	45.93	48.29	45.42	45.30	0.75
SiO ₂	41.21	35.54	36.50	0.79	0.85	1.36	0.86	0.69	0.81	0.53	0.95	1.57	0.72	3.19	0.79	0.12
TiO ₂	1.42	2.63	2.13	14.03	15.69	12.34	5.56	3.08	6.45	14.43	14.70	15.06	15.98	16.76	17.20	0.40
Al ₂ O ₃	9.29	10.93	12.10	5.47	6.77	8.34	4.53	5.06	5.44	4.07	10.59	9.27	5.23	6.71	4.98	4.17
Fe ₂ O ₃	0.15	0.17	0.19	0.10	0.13	0.10	0.07	0.07	0.08	0.05	0.10	0.12	0.08	0.05	0.10	0.14
MnO	2.92	5.09	3.17	2.48	3.41	4.90	14.63	11.70	10.60	4.85	3.76	2.82	3.92	0.58	2.40	0.50
MgO	16.11	16.21	13.64	13.92	8.67	15.52	21.23	29.41	23.32	12.79	9.58	9.44	9.12	9.95	8.00	51.35
CaO	1.17	0.40	1.14	0.25	1.48	0.16	0.13	0.13	0.22	0.18	0.17	0.39	0.25	0.19	1.04	0.02
Na ₂ O	8.56	7.21	8.57	9.17	8.00	4.43	3.24	0.29	2.77	9.49	9.39	10.85	11.57	12.01	12.75	0.10
K ₂ O	0.80	0.88	0.48	0.53	0.65	0.90	4.80	5.89	3.78	1.39	0.68	0.48	0.72	0.18	0.47	2.58
P ₂ O ₅	3.64	3.07	3.25	1.36	3.19	7.67	1.44	1.06	1.85	3.32	4.48	3.11	3.61	4.36	2.78	0.37
Pf (F+H ₂ O)	2.07	4.71	3.85	5.98	0.10	0.18	1.12	1.26	0.19	0.46	0.05	0.12	0.27	0.10	3.17	37.99
CO ₂	100.98	98.81	98.70	98.65	98.82	99.56	98.95	100.70	100.75	99.60	99.58	99.18	99.77	99.49	98.96	98.48
Total ppm	3.87	2.21	3.19	15.69	3.05	<L.D	<L.D	1.23	1.27	<L.D	<L.D	1.96	<L.D	<L.D	1.33	35.79
As	1766.00	6945.00	6729.00	11,070.00	4515.00	2253.00	2506.00	360.30	1423.00	1826.00	2289.00	3761.00	3051.00	2048.00	5060.00	4160.00
Ba	13.64	5.67	4.24	10.02	9.47	4.60	2.58	1.85	3.09	2.20	3.76	9.48	6.04	1.49	5.35	<L.D
Be	0.66	0.43	0.15	<L.D	<L.D	0.13	<L.D	<L.D	<L.D	<L.D	<L.D	0.47	<L.D	0.15	<L.D	8.48
Bi	0.37	0.79	0.66	0.40	0.28	0.32	0.12	0.14	0.10	<L.D	0.13	0.43	0.17	0.93	0.24	0.70
Cd	180.60	213.70	319.50	130.00	154.00	109.50	125.70	393.90	173.70	96.18	61.52	92.55	76.09	82.90	94.22	881.20
Ce	29.55	32.94	28.07	10.78	16.85	28.48	34.67	30.46	30.47	17.55	33.28	24.30	18.02	6.87	15.32	3.60
Co	72.22	59.30	<L.D	44.52	39.35	10.13	1566.00	413.50	574.60	17.69	6.50	4.44	9.59	<L.D	12.63	<L.D
Cr	20.17	15.67	13.74	5.67	24.64	5.31	5.01	0.78	9.86	34.83	20.43	49.67	27.97	31.58	56.74	0.09
Cs	189.30	211.60	156.70	55.19	42.58	61.54	7.74	12.25	27.41	7.96	12.96	73.74	32.44	67.35	40.74	<L.D
Cu	5.23	15.67	7.57	4.67	4.69	4.76	4.26	8.82	4.39	2.16	1.78	6.73	2.10	19.10	2.45	1.26
Dy	1.98	7.15	3.35	2.11	2.09	1.95	1.31	2.66	1.42	0.70	0.65	2.94	0.77	8.73	1.01	0.41
Er	4.03	7.50	4.82	2.57	2.60	2.91	3.42	8.03	3.51	1.77	1.23	3.48	1.38	8.50	1.63	1.40
Eu	20.84	19.72	22.04	21.71	17.77	11.46	8.05	8.15	9.17	11.66	14.04	17.28	14.23	15.18	18.03	6.28
Ga	10.24	22.44	12.44	7.49	7.35	8.12	9.59	20.83	9.56	4.75	3.42	10.14	3.89	25.62	4.43	3.62
Gd	1.35	2.16	1.98	1.29	1.37	1.46	1.66	2.15	1.86	1.07	1.05	1.34	1.10	1.98	0.97	0.41
Ge	8.00	34.28	18.46	12.46	10.19	14.18	3.00	7.12	6.65	4.79	4.60	18.27	5.76	51.16	7.88	0.12

Table 2 (continued)

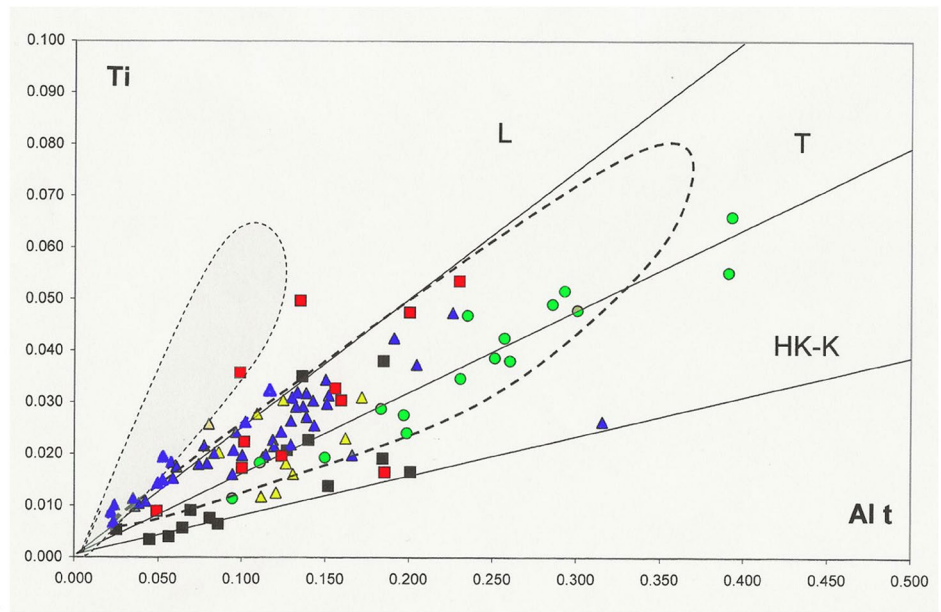
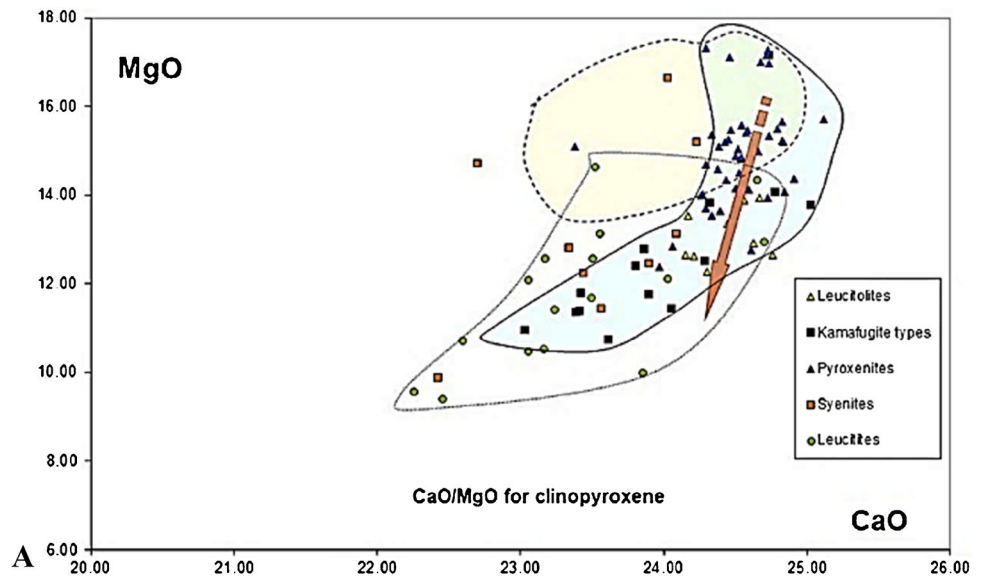
Whole-rock	Kamafu- gite-type rocks	Syenite	Leucitites	Pyroxen- ites	Leucito- lites	Leucito- lites	Carbonatite									
Ho	0.79	2.72	1.23	0.78	0.79	0.76	0.59	1.22	0.62	0.31	0.27	1.14	0.32	3.38	0.38	0.13
In	<L.D	0.11	0.11	<L.D	<L.D	0.09	<L.D	0.07	<L.D	<L.D	<L.D	0.07	<L.D	0.10	<L.D	<L.D
La	84.84	94.96	135.90	70.09	81.02	45.48	57.25	202.40	88.64	47.69	30.25	41.66	37.17	18.87	48.99	662.00
Lu	0.25	0.91	0.50	0.30	0.28	0.24	0.12	0.21	0.14	0.07	0.08	0.38	0.09	1.07	0.15	0.03
Mo	0.74	0.81	2.16	13.32	0.71	<L.D	<L.D	<L.D	<L.D	<L.D	0.63	<L.D	1.13	0.56	0.61	1.38
Nb	22.24	23.74	100.60	25.16	24.51	7.41	3.33	1.06	1.28	0.58	3.46	12.63	7.72	14.51	12.49	83.65
Nd	96.17	125.80	145.90	63.26	62.62	59.72	78.44	203.50	87.05	48.25	30.47	56.51	35.84	95.31	43.15	138.50
Ni	22.02	27.62	10.08	16.05	22.29	24.57	135.10	71.76	75.58	19.93	21.71	8.20	16.84	4.50	11.02	4.52
Pb	103.03	63.00	34.19	243.43	76.05	12.46	2.40	4.26	5.18	2.15	5.01	61.31	15.04	14.07	18.29	1618.68
Pr	23.11	27.91	38.10	15.74	17.29	13.05	17.83	48.47	21.28	11.65	7.40	12.29	9.15	15.95	10.95	62.68
Rb	363.20	345.30	275.80	238.60	962.50	386.90	202.90	30.34	232.00	836.70	873.70	749.20	721.80	800.40	850.10	3.93
Sc	<L.D	22.46	<L.D	<L.D	12.72	23.93	36.23	63.78	44.69	23.35	21.45	13.86	18.93	24.19	<L.D	<L.D
Sb	0.41	0.17	0.31	1.90	0.40	<L.D	<L.D	<L.D	<L.D	<L.D	<L.D	0.11	<L.D	<L.D	0.20	0.30
Sm	17.78	29.06	22.25	11.66	10.82	11.82	15.24	34.76	15.17	7.81	5.36	13.10	6.08	30.13	7.32	8.24
Sn	4.91	13.05	7.62	4.26	4.19	7.45	1.26	3.50	4.60	2.84	3.50	8.25	2.96	20.36	3.23	0.45
Sr	1626.00	740.20	423.60	2256.00	3592.00	1508.00	778.10	1517.00	1325.00	581.30	514.80	811.00	978.80	471.40	1046.00	11,960.00
Ta	2.66	3.61	8.09	1.61	1.83	1.03	0.34	0.37	0.36	0.06	0.33	1.24	0.68	3.19	1.11	0.04
Tb	1.19	3.05	1.59	0.94	0.95	1.00	1.01	2.18	1.03	0.52	0.40	1.33	0.46	3.60	0.53	0.37
Th	39.49	48.75	74.22	41.76	41.92	20.49	10.12	36.11	16.35	11.78	10.91	22.59	15.63	22.03	22.43	0.10
Tm	0.26	1.00	0.48	0.30	0.30	0.26	0.15	0.28	0.16	0.08	0.08	0.41	0.10	1.19	0.14	0.04
U	8.22	11.27	20.10	18.53	6.88	3.94	1.68	2.64	1.59	1.16	1.71	6.73	3.70	7.23	8.85	7.81
V	239.20	332.90	522.50	214.40	152.50	140.80	65.70	78.96	92.63	52.80	127.50	207.60	79.04	175.40	155.50	331.50
W	1.16	0.88	1.55	25.35	0.76	<L.D	<L.D	0.12	<L.D	<L.D	0.13	0.21	0.16	0.21	0.14	0.30
Y	24.41	78.22	40.02	25.43	25.59	22.03	17.03	34.24	18.23	8.54	7.80	31.97	9.11	90.88	12.22	3.91
Yb	1.65	6.40	3.29	2.00	1.93	1.65	0.83	1.55	0.94	0.48	0.52	2.63	0.61	7.44	0.93	0.22
Zn	118.90	108.70	43.73	59.34	80.97	47.61	41.12	27.94	34.76	19.09	58.40	87.97	37.84	26.25	59.29	41.58
Zr	495.30	1307.00	1000.00	609.00	414.40	463.10	97.79	163.00	172.20	104.10	132.70	580.40	177.80	1524.00	341.70	9.04
CIPW norm																
Quartz	0.00	0.00	0.00	0.00	0.00	0.00	0.00	0.00	0.00	0.00	0.00	0.00	0.00	0.00	0.00	0.00
Plagioclase	5.96	6.74	4.18	5.58	11.63	18.96	4.00	7.85	6.82	9.81	10.67	6.50	7.07	8.57	2.57	
Orthoclase	0.00	0.00	0.00	17.92	36.24	4.68	0.00	0.00	0.00	2.54	0.00	0.00	0.00	0.00	1.63	
Nepheline	5.36	1.83	5.23	1.15	6.78	0.73	0.60	1.01	0.60	0.83	0.78	1.79	1.15	0.87	4.77	
Leucite	40.80	37.85	41.80	35.50	10.08	18.29	16.61	13.75	1.57	43.13	44.99	51.53	55.55	56.96	60.99	
Kalsilite	0.00	0.00	1.58	0.00	0.00	0.00	0.00	0.00	0.00	0.00	0.00	0.00	0.00	0.00	0.00	0.00

Table 2 (continued)

Whole-rock	Kamafu- gite-type rocks	Syenite	Leucitites	Pyroxen- ites	Leucito- lites	Carbonatite
Corundum	0.00	0.00	0.00	0.00	0.00	0.00
Diopside	13.94	18.87	22.15	41.77	33.45	11.75
Hypersthene	0.00	0.00	0.00	0.00	0.00	0.00
Wollastonite	0.00	0.00	0.00	0.00	0.03	0.00
Olivine	6.66	1.53	3.13	14.59	0.00	0.00
Larnite	12.20	0.00	0.00	3.10	0.00	3.54
Acmite	0.00	0.00	0.00	0.00	0.00	0.00
K ₂ SiO ₃	0.00	0.00	0.00	0.00	0.00	0.00
Na ₂ SiO ₃	0.00	0.00	0.00	0.00	0.00	0.00
Rutile	0.00	0.00	0.00	0.00	0.00	0.00
Ilmenite	2.70	1.50	1.61	1.63	1.01	1.50
Magnetite	2.70	1.58	1.96	1.32	1.17	1.45
Hematite	0.00	0.00	0.00	0.00	0.00	0.00
Apatite	1.85	1.23	1.51	11.12	3.22	1.09
Zircon	0.10	0.12	0.27	0.27	0.01	0.07
Perovskite	0.00	0.00	0.00	0.00	0.00	0.00
Chromite	0.01	0.01	0.00	0.34	0.00	0.00
Calcite	4.71	13.60	0.23	2.55	1.05	7.21
Total	96.99	98.59	95.59	97.90	96.25	96.57
Fe ₃ +/(Fe ₃ +Fe ₂)	20.0	19.9	20.0	20.1	19.9	20.1
Mg/ (Mg+Fe ₂)	38.4	47.3	50.0	86.5	70.3	48.8
DI	52.12	60.2	64.7	21.2	56.3	70.0
agpa. Index	0.82	0.74	0.71	0.67	0.73	0.90

*EI**, hydrothermalized leucite matrix of the phreato-magmatic deposit; *DI*, differentiation index of Thornton and Tuttle (1960); *agpa. Index*, index of agpaicity

Fig. 5 **A** MgO versus CaO diagram (wt. %) for clinopyroxene. Arrow, evolution trend in pyroxenite xenoliths: the dotted fencing yellow field is for kamafugite from Prelević et al. (2005); the two other fields are for pyroxenite, kamafugite-type and leucitilites of the present study and leucitites of the present study. **B** Ti/Al_t (a.p.f.u.) diagrams for clinopyroxene. L, lamproitic field after Mitchell and Bergman (1991); T and HK-K, transitional high-K and K series of Italian volcanic magmatism (after Perini and Conticelli 2002). Dotted fields: Cpx respectively from lamproites and kamafugites after Prelević et al. (2005)



495 2005; Caran 2016). Ba and Al-Si coupled substitution
 496 occurred exclusively in phlogopite when it crystallized
 497 before feldspar under high P_{H_2O} , and in strongly silica-
 498 deficient magmas, prohibiting feldspar crystallization. It
 499 is also favored by a relatively high fO_2 and P_{H_2O} (Edgar
 500 and Arima 1981). This is true for kamafugite, nephelin-
 501 ite, ankaratrite, and carbonatite. On the other hand, when
 502 alkali feldspar crystallizes, as it is in the feldspar-bearing
 503 syenite of the present study, Ba is preferentially incorpor-
 504 ated into hyalophane and phlogopite remains Ba-poor.

Garnet

Garnet is strongly zoned from black core to brown-yellowish
 rim. Andradite (81–87%) and almandine (5–15 wt.%) are
 its main components (Appendix 1G). Black crystal cores
 are composed of melanite with > 15 wt.% TiO_2 . Yellowish
 rims are Ti depleted and more Fe- and Ca-enriched with the
 increase of Fe-andradite and almandine components. MgO
 remains very low (< 1.3 wt.%) and decreases from garnet of
 kamafugite to those of syenite xenoliths. Melanite appears

505
 506
 507
 508
 509
 510
 511
 512
 513

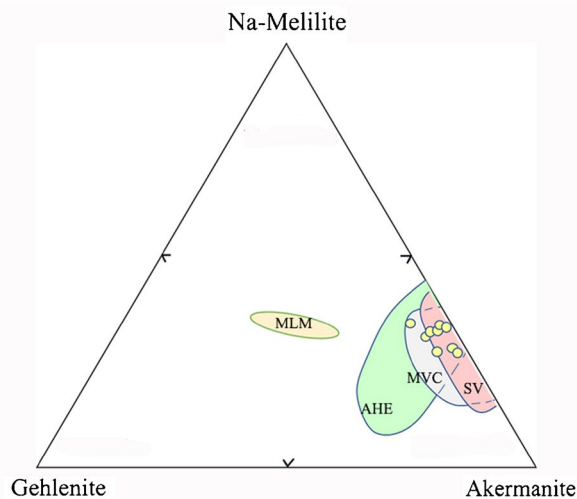


Fig. 6 Melilite compositions in the gehlenite–akermanite–Na melilite ternary diagram. Yellow dots, present study; SV field, San Venanzo volcanics, Intra-mountain Ultra-alkaline Province, Italy; AHE field, Alban Hill Ejecta, Roman Province, Italy; MVC, Montefiascone clinopyroxenite xenoliths, Roman Province, Italy; MLM, melilite-bearing leucitite, Meşebaşı area, Afyon K-UK Province Anatolia (after Stoppa et al. 2003a, b, c; Akal 2003)

514 to be a systematic phase in the Potassic-Ultrapotassic Afyon
 515 Province magmatism and has been also described in melilite
 516 leucitites, melanite-bearing xenoliths from the Balçıkhisar
 517 area (Akal 2003; Akal et al. 2013), and in other localities
 518 of the western Taurides ultrapotassic volcanism (Prelević
 519 et al. 2015). Garnet is also present in leucitite and carbon-
 520 atite inclusions from the Senirkent area of the Isparta Angle
 521 (Elitok 2019). Melanite has also been observed in other
 522 Ultrapotassic Provinces, such as in xenoliths of the Alban
 523 Hills ultrapotassic ejecta, Roman Province, Italy (Federico
 524 et al. 1994).

525 **Other minerals**

526 Apatite is observed in all xenolith groups and in leucitite.
 527 The composition variations (Appendix 2A, B) concern only
 528 SrO which varies between 0.3 and 1.2 wt.% but reaches up
 529 to 6.5 wt.% in the syenite. Silica is in the range 0.6–1.9
 530 wt.%, but reaches 2.8 wt% in the apatite of carbonatite. F is
 531 relatively abundant with 1.5 to 2.4 wt.%, reaching 3.2–3.8
 532 wt.% in the apatite of the syenite and leucitite. Apatite also
 533 contains REE, particularly the apatite of the carbonatite,
 534 with 1.2–1.3 wt.% of Ce₂O₃.

535 Magnetite has an ulvospinel component that varies widely
 536 from 39 to 4% (Appendix 2C). The Mn jacobsonite and mag-
 537 nesioferrite components reach 9% and 15% respectively in
 538 the carbonatite magnetite. The early crystallization of mag-
 539 netite in some leucitolites seems to be related to oxidising

540 conditions. It would also be related to the H₂O/CO₂/F ratio
 541 in the dissolved fluid phase, but we have no precise informa-
 542 tion on this ratio and its evolution.

543 Calcite forms the peperite matrix and is the major min-
 544 eral of the carbonatite xenolith. Microprobe analysis results
 545 (Appendix 2D) show that it is almost pure calcite with very
 546 low MgO content even in the carbonatite. However, SrO can
 547 reach 2.2 wt.% in the calcite of the carbonatite.

548 **Preliminary geochemical results**

549 **Major elements**

550 All the studied felsic rocks belong to strongly silica-
 551 undersaturated series, and are foidite-foidolite type rocks
 552 (Table 2). Many plutonic xenoliths found in the Eğirdir area
 553 have cumulated characters such as the ultramafic pyroxenite
 554 with one or two liquidus main phases (clinopyroxene and
 555 phlogopite) and the leucitolite xenoliths with two main lay-
 556 ered phases (leucite and clinopyroxene). Kamafugite-type
 557 xenoliths and feldspath-bearing syenite, exhibiting micro-
 558 granular or coarse-grained homogeneous textures, are closer
 559 to liquid compositions. More appropriate specific classifica-
 560 tion schemes for ultrapotassic rocks than TAS diagram (Le
 561 Maitre 2002) are usually used (Sahama 1974; Foley et al.
 562 1987; Foley 1992b; Woolley et al. 1996).

563 The microgranular and texturally homogeneous coarse-
 564 grained xenoliths (Table 2, Figs. 8, 9) have MgO ≥ 3 wt.%,
 565 K₂O > 7 wt.%, and high CaO and are poor in Al₂O₃ and
 566 Na₂O (< 1.2 wt.%). They show the lowest value of SiO₂,
 567 intermediate values of CaO and K₂O, and are relatively rich
 568 in FeOt and TiO₂. They are evolved with a DI (Thornton
 569 and Tuttle 1960) > 45 and have no modal olivine like some
 570 ultrapotassic plutonic rocks of the Roman Province, Italy
 571 (Peccerillo et al. 1984; Peccerillo 1990). They belong to the
 572 melilite-, leucite-, and kalsilite-bearing kamafugite group,
 573 according to their major element characters (Table 2; Figs. 8,
 574 9). These xenoliths are strongly silica-undersaturated (see
 575 CIPW norms, Table 2) with normative leucite, nepheline,
 576 and sometimes normative kalsilite. They are very calcic with
 577 modal melilite, almost always with normative larnite (some-
 578 times > 10 wt.%) and normative calcite.

579 The pyroxenite xenoliths are the most enriched in MgO,
 580 CaO, and P₂O₅ due to clinopyroxene and apatite (Figs. 8,
 581 9; Table 2). Their variable K₂O is essentially related to
 582 the occurrence of phlogopite. They are potentially silica-
 583 undersaturated but much less than kamafugite and leucitolite
 584 xenoliths (Table 2).

585 The leucitolite xenoliths plot in the leucitite field (Fig. 9).
 586 These rocks are relatively poor in MgO, and extremely rich
 587 in K₂O and Al₂O₃, with a very high K₂O/Na₂O ratio (Fig. 9).
 588 The opposite variations between K₂O, Al₂O₃, and FeOt,
 589

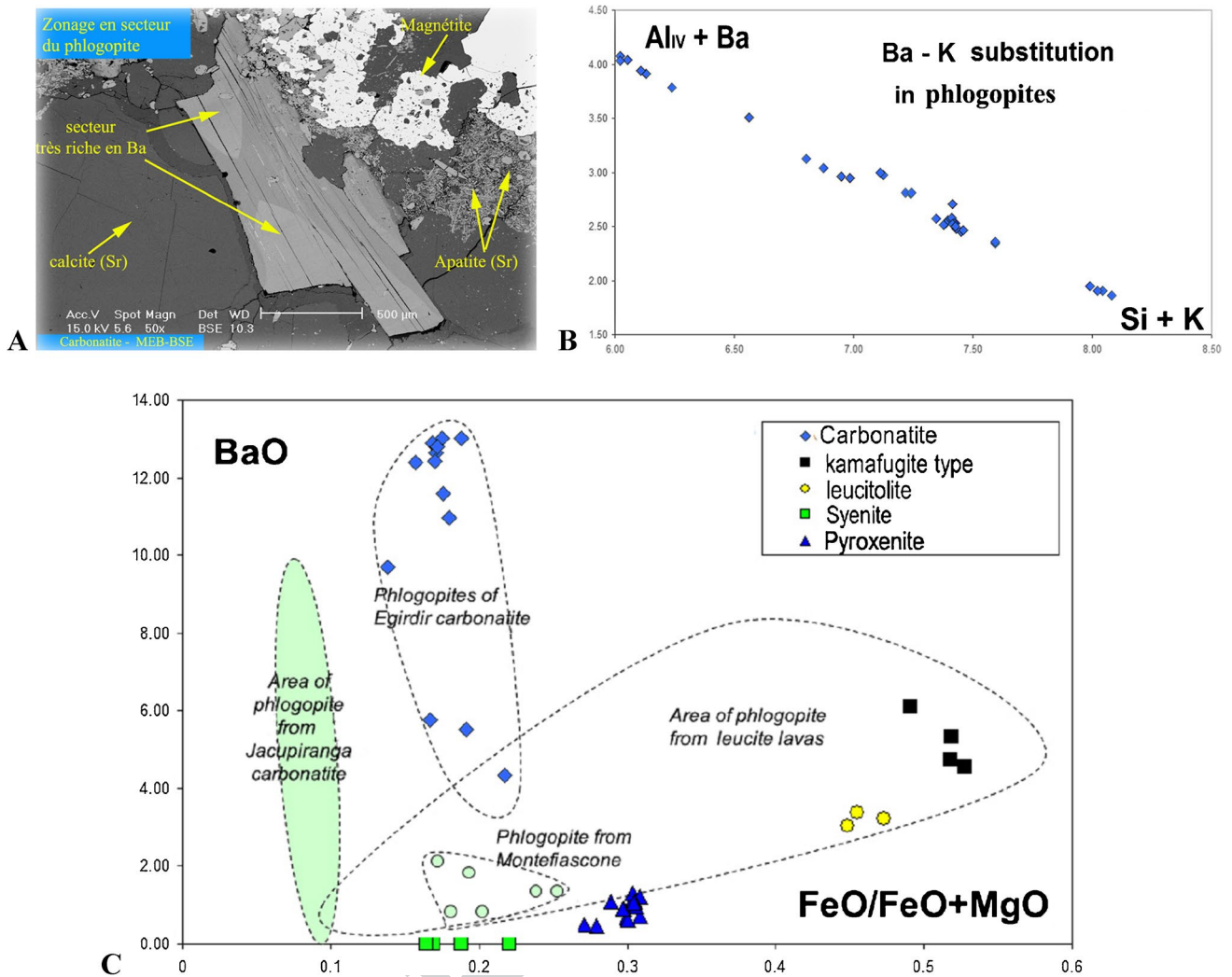


Fig. 7 Composition variations of phlogopite. **A** Sector zoning in phlogopite of the carbonatite xenolith, MEB back-scattered picture. **B** Ba-K substitution in phlogopite from Eğırdir xenoliths. **C** BaO versus FeO/FeO+MgO ratio in phlogopite of carbonatite xenolith and

other xenoliths compared to phlogopite of the Jacupiranga carbonatite and phlogopite of leucite lavas (after Gaspar and Wyllie 1982). Green dots, phlogopite of Montefiascone clinopyroxenite, Italy (after Stoppa et al. 2003a, b, c)

589 TiO₂, and MgO contents depend on the leucite/mafic phases
 590 (clinopyroxene, garnet, Fe-Ti oxides) ratio in this group, in
 591 relation with mineral segregation process. The leucitolite
 592 xenoliths (Fig. 9) are always very depleted in Na₂O by compar-
 593 ison to the melilite-bearing leucitites and other previously
 594 studied Afyon leucitites (Akal 2003; Prelević et al.
 595 2015).

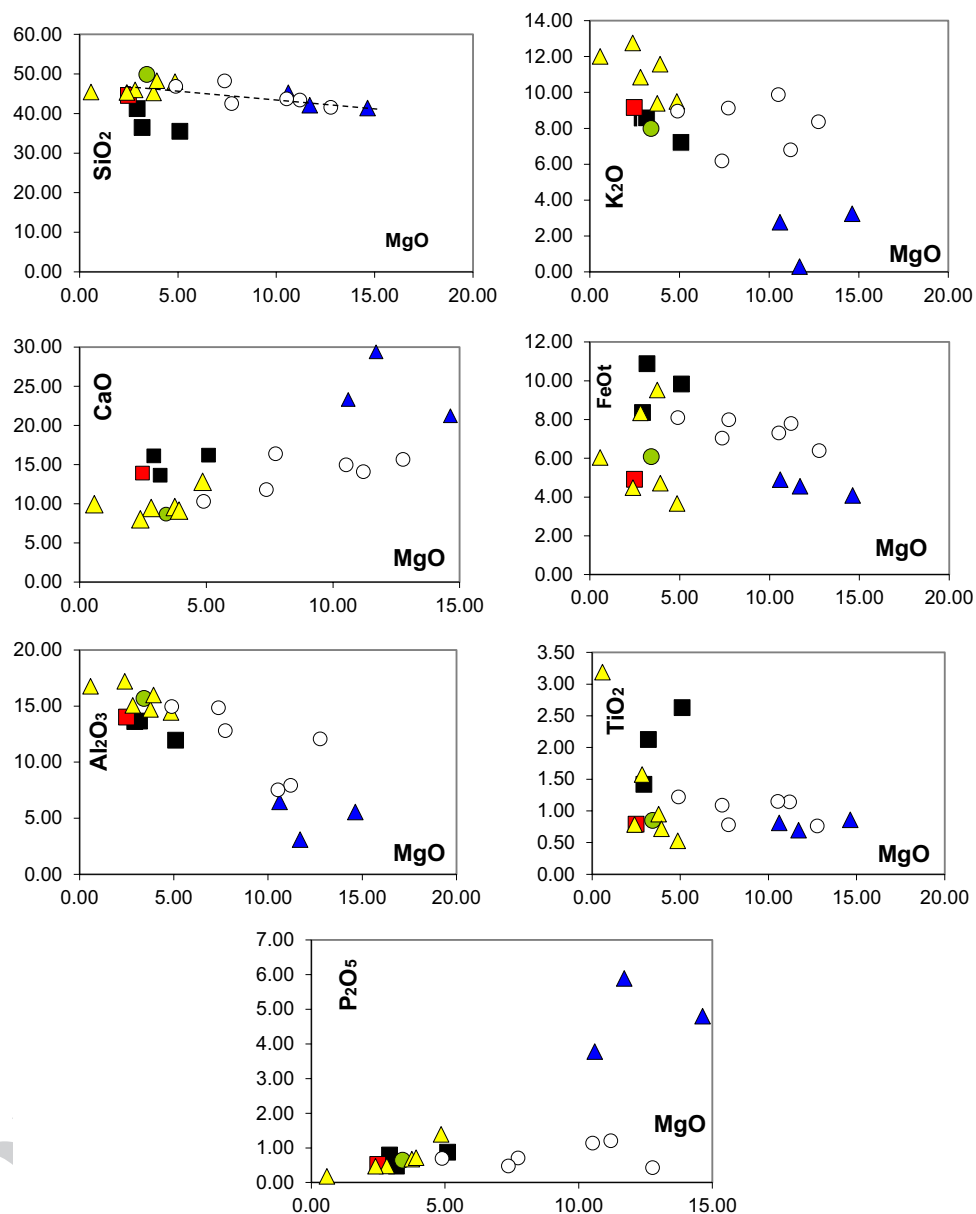
596 The observed gaps between the main xenolith groups
 597 (Figs. 8, 9) can be related to cumulative processes involv-
 598 ing mainly clinopyroxene, apatite, and leucite, as indicated
 599 by the textural characteristics of pyroxenites and leucito-
 600 lites. In almost all Harker diagrams (Fig. 8), the xenoliths
 601 from the Alban Hills ejecta, Italy (Peccerillo et al. 1984;
 602 Federico et al. 1994) plot in the gap observed between
 603 pyroxenite and leucitolite groups. They are P₂O₅-poor

604 compared to the pyroxenite group of Eğırdir. The KLT
 605 kalsilitite from Alban Hills ejecta (Figs. 8, 9) plots close
 606 to the kamafugite-type xenoliths of Eğırdir. The assumed
 607 primary kamafugite “KAM” composition proposed by
 608 Prelević et al. (2015) also plots between the pyroxenite
 609 and leucitolite groups (Fig. 9).

610 The hyalophane-bearing syenite and Eğırdir leucite
 611 compositions are close to the leucitolite group, but with
 612 lower K₂O and TiO₂ + FeO values.

613 The carbonatite xenolith is very poor in Na₂O and MgO
 614 (Table 2) and belongs to the calcio-carbonatite type. The
 615 P₂O₅ is very high (2.58 wt.%) due to the presence of apa-
 616 tite clusters, which must be considered for the interpreta-
 617 tion of REE and other trace elements in the rock.

Fig. 8 Major elements versus MgO. Blue triangle, pyroxenite. Yellow triangle, leucitilite. Black square, kamafugite type. Red square, hyalophane-bearing syenite. Green dot, Egirdir leucitite. Open dot, plutonic xenoliths from the Alban Hills Ejecta, Italy

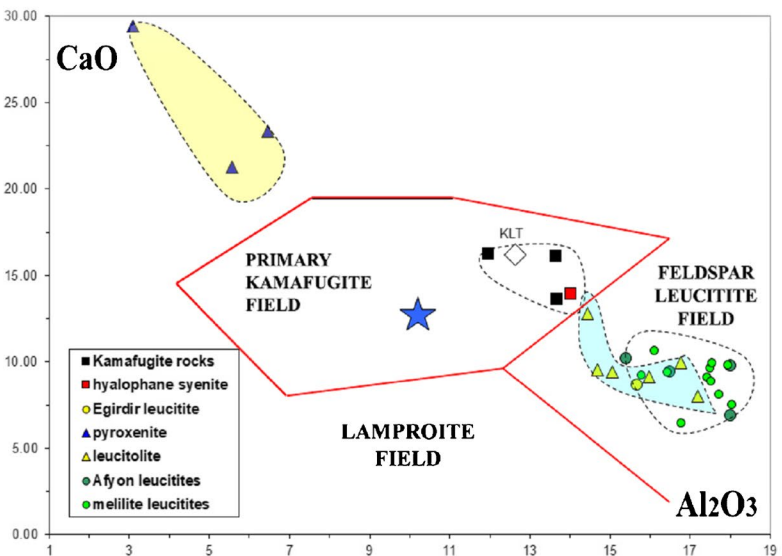
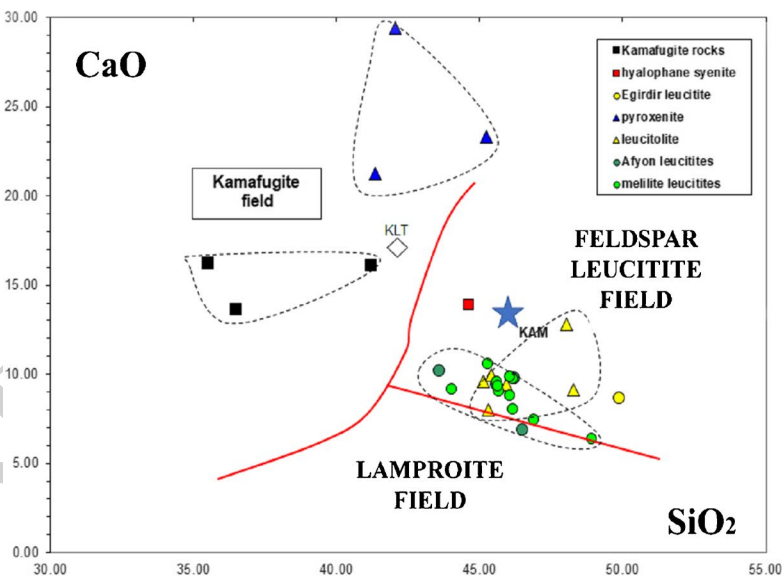
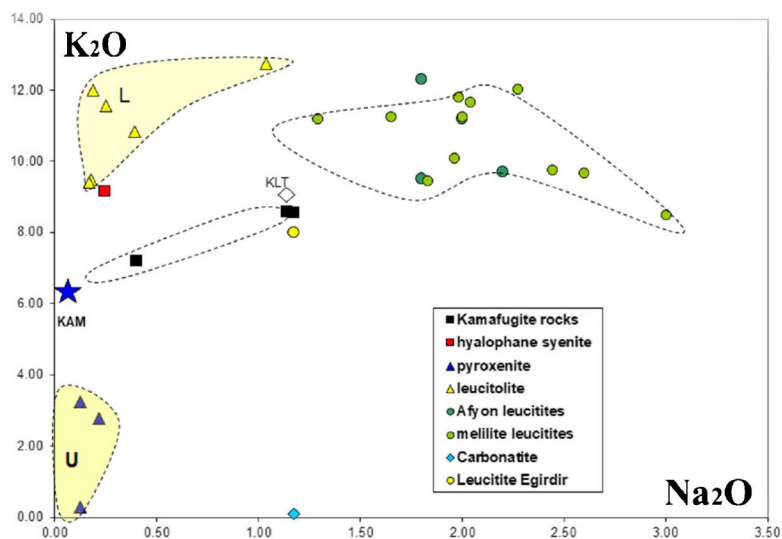


618 **Trace elements**

619 The spidergrams normalized to the primitive mantle
 620 (Fig. 10A) for trace elements (Table 2) are used for the
 621 feldspar-bearing syenite, leucitites, and kamafugite-type
 622 xenoliths that are close to liquid compositions. The syenite
 623 and leucitite patterns are very similar, and show a rela-
 624 tively high LILE to HFSE ratio. The negative Ta, Nb, and
 625 Ti anomalies are present but are moderate (weak in the
 626 case of Hf), while Zr displays a weak positive anomaly.
 627 The kamafugite-types display the same negative anom-
 628 alies. They are globally enriched in REE relative to the
 629 syenite and leucitite. The negative Sr anomaly is particu-
 630 larly pronounced for two kamafugite-type xenoliths, prob-
 631 ably related to early apatite fractionation. All the rocks

632 have a prominent Pb positive peak. All these geochemical
 633 features have been also noted for ultrapotassic magmatism
 634 of the Roman Province, Italy (Conticelli et al. 2013, 2015).
 635 They are related to an orogenic or post-orogenic signature
 636 with a crustal material assimilation into the upper mantle
 637 during a previous subduction process. However, there are
 638 some discrepancies: Ba is not very depleted and there is
 639 no clear positive Th and Cs peaks. The same geochemical
 640 characters have been observed in the Ultrapotassic-Potas-
 641 sic Afyon volcanic Province (Prelević et al. 2015). The
 642 trace element patterns of the studied xenoliths are very dif-
 643 ferent from those of intraplate ultrapotassic rocks, similar
 644 to the Roman Province (Conticelli et al. 2015). Looking at
 645 the REE patterns (Fig. 11), kamafugite-type xenoliths are
 646 enriched in REE, especially HREE, compared to leucitite

Fig. 9 Major element diagram with kamafugite, leucitite and lamproite fields after Foley (1987). Blue star, assumed primary kamafugite magma after Prelević et al. (2015). Open diamond, KLT kalsilitolite xenolith from Alban Hills ejecta (Federico et al. 1994). Afyon leucitites are from Prelević et al. (2015). Melilite leucitite are from Akal (2003), Akal et al. (2013)



UNCORRECTED

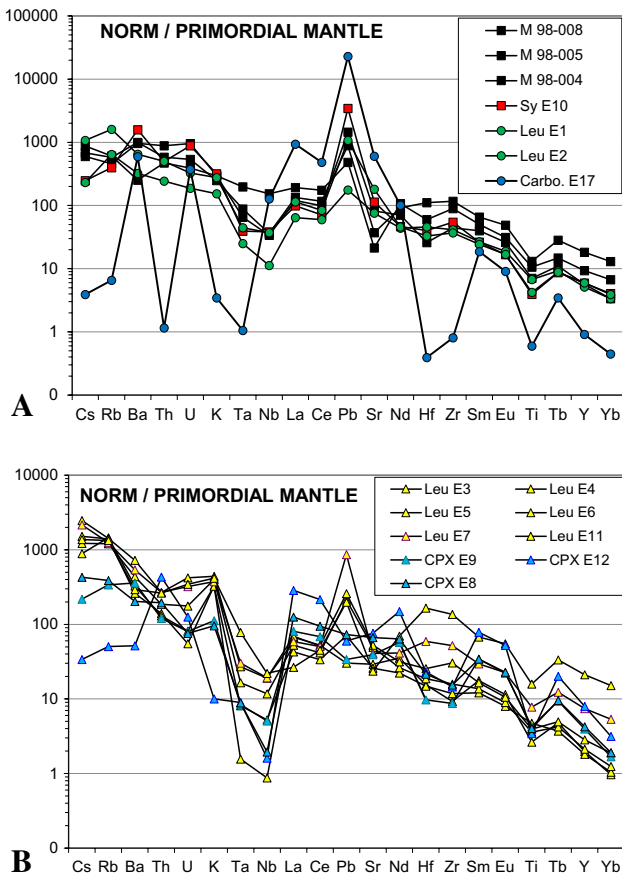


Fig. 10 Trace elements normalized to primordial mantle. **A** Patterns of kamafugite-type (M, black squares), syenite (Sy), leucitite (Leu), and carbonatite (Carbo) xenoliths. **B** Patterns of leucitolite (Leu) and clinopyroxenite (CPX) xenoliths. Normalizing values from Sun and McDonough (1989)

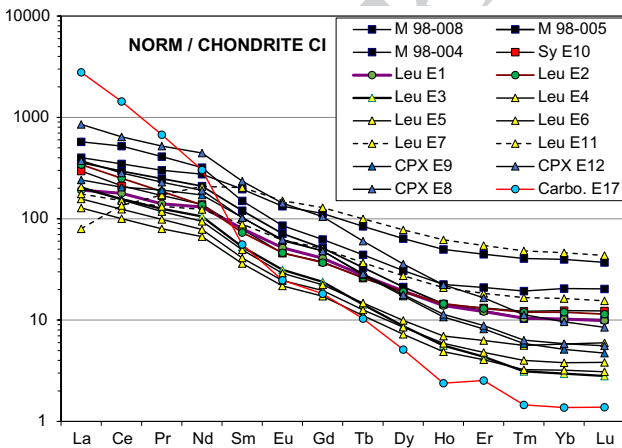


Fig. 11 REE/chondrite CI normalized patterns. Same rock references as Fig. 10

and syenite (Figs. 10, 11). All the trends show no positive or negative Eu anomaly.

Spidergrams are less suited to xenoliths involving cumulative processes (pyroxenite and leucitite xenoliths), but the patterns provide a simple overall view of the main trace elements and can show the possible effects of mineral fractionation on the parent liquids. The pyroxenite xenoliths are depleted in HFSE, Pb, and LILE (including Pb) relative to REE and have enriched HREE relative to LREE, due to their high but variable modal apatite and pyroxene fractions (Figs. 10B, 11). They are Th-enriched. Rb and Ba are variable and enriched together with K in two pyroxenites, due to the third mineral to crystallize which is phlogopite.

The trace element patterns of the leucitite xenoliths are globally similar (Figs. 10B, 11) and characterized by a global depletion in REE, Ta, Nb, and Ti when compared to the patterns of leucitite and kamafugite type. The leucitites are globally enriched in LILE relative to pyroxenites, and K. However, notable variations of HFSE troughs and HREE/LREE ratio in this leucitite group seem to be very dependent upon the leucite/clinopyroxene ratio and garnet content. Two garnet-rich leucitites (Fig. 11) are strongly enriched in HREE, Zr, and Hf relatively to LREE. The role of garnet is probably crucial for these samples, and is consistent with the trace element patterns of garnet published by Prelević et al. (2015). A prominent peak of Pb is always seen for the most leucite- and garnet-enriched leucitites, which is a difference with the pyroxenite group.

The trace element pattern of the carbonatite (Figs. 10A, 11) shows a strong LREE/HREE fractionation pattern and is very depleted in HFSE, except for Nb, and is also depleted in K, Rb, and Th relative to U and Ba. It has the most prominent Pb peak. This pattern has nothing to do with that of intraplate carbonatites, but shows similarities with those of sandstones, pelites, and especially limestones of the past and present Mediterranean alpine area (see the trends published by Conticelli et al. (2015 and ref. therein)), with very high peaks for U, Pb, and Sr and deep troughs for K, Ta, Hf, Zr, and Ti. However, apatite, which forms clusters in the carbonatite xenolith, is the first mineral that can explain the LREE/HREE enrichment of the carbonatite. Moreover, the spidergrams of apatite from the Potassic Ultrapotassic Afyon volcanic Province (Prelević et al. 2015) show the same LREE/HREE enrichment and deep troughs for Ti, Zr, Ta, and Rb. The only discrepancy concerns Th, which is very low in this carbonatite xenolith. This depletion eventually may be linked to pneumatolytic reworking and escape of Th during the phreatomagmatic event, a process that could be considered as viable for a 10-cm-sized xenolith.

698 **Stable isotope data on calcite**

699 ¹⁸O and ¹³C stable isotope analyses have been carried out on
 700 calcite extracted from the carbonatite xenolith, the peperite
 701 matrix, the hyalophane-bearing syenite, and two limestones
 702 from the surrounding basement that has been cut and covered
 703 by the volcanoclastic deposit (Table 3, Fig. 12). Analy-
 704 ses are reported on the $\delta^{18}\text{O}$ versus $\delta^{13}\text{C}$ diagram (after Bell
 705 2005; Doroshkevich et al. 2010). The $\delta^{13}\text{C}$ isotopic signa-
 706 tures of calcite from the carbonatite xenolith, the peperite
 707 matrix, and the hyalophane-bearing syenite are negative and
 708 are distinct from the $\delta^{13}\text{C}$ measured on the limestones from
 709 the basement. The $\delta^{13}\text{C}$ and $\delta^{18}\text{O}$ values of the carbonatite
 710 are close to the limit values for the primary carbonatite field
 711 (PCF, Fig. 12). This means that a mantle signature, with

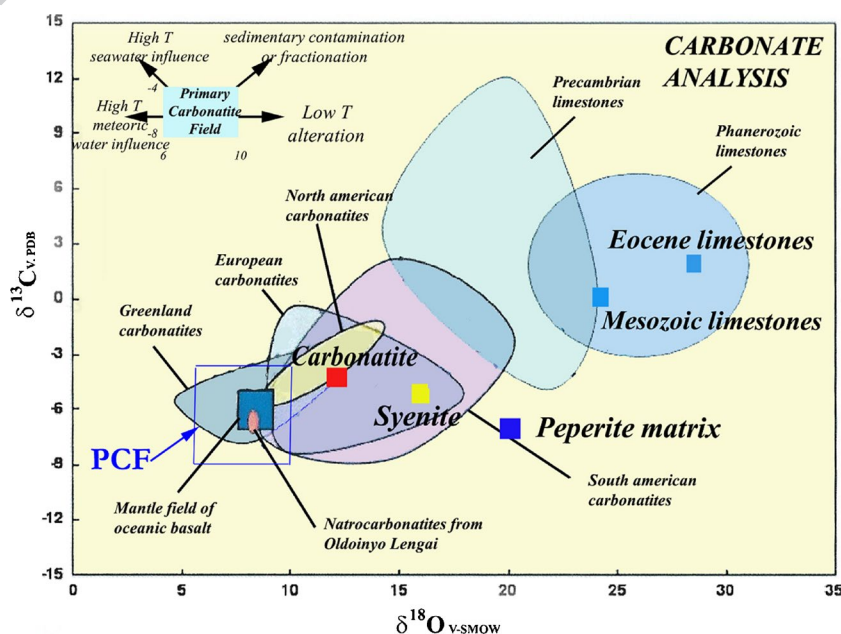
slight modification by fractionation or contamination, can be
 712 considered for the carbonatite xenolith. Similarly, the $\delta^{13}\text{C}$
 713 of the calcite found in the syenite is also compatible with a
 714 primary origin of the CO₂-rich fluid component dissolved
 715 in the magma parent and plots within the so-called Euro-
 716 pean carbonatite field. However, the $\delta^{18}\text{O}$ is significantly
 717 higher, which can be ascribed to a contamination during a
 718 low-temperature alteration process. The $\delta^{18}\text{O}$ of the peperite
 719 matrix is much higher and disconnected from its $\delta^{13}\text{C}$ that
 720 remains low, which can be ascribed to a main contamina-
 721 tion process at a low temperature involving meteoritic H₂O
 722 during the volcanic event. A carbonatitic fluid interaction
 723 has been proposed in some peperite belonging to the Ceno-
 724 zoic French Limagne phreatomagmatism (Bailey et al. 2006;
 725 Chazot and Mergoïl-Daniel 2012), which is an alternative
 726

Table 3 $\delta^{13}\text{C}$ and $\delta^{18}\text{O}$ stable isotope measures on carbonates

Rock sample	Processing	d13C/PDB	d18O/PBD	d18O/SMOW*	Mineral specificity
E17 carbonatite	H3PO4 24 h à 25 °C	-4.60	-17.76	12.60	calcite
E17 carbonatite	H3PO4 15 Days at T=25 °C	-4.60	-17.82	12.54	calcite + Mg-carbonate
E10 syenite	H3PO4 15 Days at T=25 °C	-5.30	-13.81	16.67	calcite + Mg-carbonate
E10 syenite	H3PO4 24 h at T= 100 °C	-5.55	-14.94	15.51	all carbonates
SE17 limestone	H3PO4 15 Days at T=25 °C	1.94	-2.34	28.50	calcite + Mg-carbonate
SE08 limestone	H3PO4 15 Days at T=25 °C	-0.83	-6.41	24.30	calcite + Mg-carbonate
PEP peperite matrix	H3PO4 15 Days at T=25 °C	-6.8	-9.65	20.96	calcite + Mg-carbonate

$\delta^{18}\text{O}$ SMOW calculated after Coplen et al., 1983. Measure precisions: $\delta^{13}\text{C}/\text{PDB} \pm 0.1$; $\delta^{18}\text{O}/\text{PBD} \pm 0.2$

Fig. 12 $\delta^{13}\text{C}$ versus $\delta^{18}\text{O}$ stable isotope composition of calcite from xenoliths and limestones. Calcite has been extracted from two plutonic xenoliths (carbonatite and syenite), the peperite matrix at the bottom of the volcano-clastic deposit, and two limestones (Mesozoic limestone and Eocene lacustrine) of the surrounding basement. PCF, primordial carbonatite field



727 from the classical origin of peperite. It is difficult to rule out
 728 the prevalent low-T interaction process between the leucite
 729 magma, meteoritic water, and limestones or lacustrine
 730 that raises the $\delta^{18}\text{O}$ but not the $\delta^{13}\text{C}$ for the calcitic matrix
 731 of the peperite. In the other hand, the low $\delta^{13}\text{C}$ can also be
 732 explained by the presence of a juvenile CO_2 -rich fluid in
 733 relation with the leucite lava or/and a separate carbonatitic
 734 magma.

735 **Discussion**

736 **Xenolith mineral parageneses and their origin**

737 Textures and restricted mineral paragenesis of pyroxenites
 738 and leucitolites (one to three euhedral major phases),
 739 and geochemical gaps existing between pyroxenites and
 740 leucitolites on the one hand, and syenite, kamafugites,
 741 and leucitites on the other hand, suggest that pyroxenites
 742 and leucitolites are assumed to be cumulates derived from
 743 underlying magma intrusions. The term of autolith would
 744 be better than xenolith for these two groups of rocks as it
 745 has been used for the autoliths from the Kilombe volcano,
 746 Kenya Rift, and the Ilimaussaq autoliths, Greenland (Ridolfi
 747 et al. 2006; Schönerberger et al. 2006). Cumulate-type rocks
 748 are known in ultrapotassic provinces, such as the Malawi
 749 ring complexes, in particular the ultrapotassic Mlindi ring
 750 complex (Laval and Hottin 1992). Trace element patterns of
 751 pyroxenite and leucitolite also show that their bulk composi-
 752 tions are a direct expression of the ratio of mafic and felsic
 753 mineral. Apatite, clinopyroxene, phlogopite, and leucite are
 754 the major mineral phases that crystallized in the magma at
 755 depth, in good agreement with the differentiation process
 756 suggested by Prelević et al. (2015).

757 Small xenoliths of kamafugite affinity are very enriched
 758 in early melilite crystals and some leucitolite cumulates are
 759 very garnet-enriched, which suggests that some garnet- or
 760 melilite-enriched segregations or layers formed during their
 761 crystallization.

762 Kamafugite-type and syenite xenoliths show homoge-
 763 neous fine-grained porphyritic textures, a common feature
 764 observed not only in small dykes, but also on the chilled
 765 margins of intrusions. Coarse-grained kamafugite-type
 766 xenoliths never show layering features or crystal segrega-
 767 tion, indicating that they probably represent evolved liquids
 768 injected and crystallized at depth in the crust.

769 **Implications of experimental studies**

770 The variable mineral paragenesis of the studied xenoliths is
 771 relevant to the complex system kalsilite-forsterite-larnite-
 772 quartz tetrahedron and related subtetrahedra (Yoder 1986;
 773 Gupta 2015) and has been experimentally investigated for

a long time (Gupta et al. 2006; Edgar et al. 1976; Gupta and
 Yagi 1980; Veksler et al. 1998; Gupta 2015 and ref. therein).
 In the Eğirdir xenoliths, the presence of phlogopite and lack
 of olivine fit well in the phlogopite-kalsilite-clinopyroxene-
 leucite-melilite-feldspar sub-tetrahedra, with mutual exclu-
 sion between melilite and feldspar, as it is observed in
 melilite-bearing kamafugite-type and feldspar-bearing syenite
 xenoliths. However, the natural paragenesis system is more
 complicated than the experimental system because Fe and Ti
 were not considered. The later elements probably complicated
 the paragenesis with crystallization of FeTi-oxides and
 garnet. Heteromorphic relations with incomplete reactions
 (Yoder 1986) in kamafugite magmas can also complicate the
 paragenesis of the rocks during crystallization.

Conditions of crystallization and fractionation processes

The modal variations depicted in the xenoliths show that
 the early crystallizations of melilite, clinopyroxene, apatite,
 and phlogopite, followed by leucite, play the major role in
 the differentiation process, in good agreement with experi-
 mental studies.

Early crystallization of phlogopite rather than olivine in
 phlogopite-bearing pyroxenite cumulates, and early Ti-Fe
 oxides associated with clinopyroxene phenocrysts in subvol-
 canic kamafugite-type are symptomatic of relatively elevated
 partial $P_{\text{H}_2\text{O}}$ and oxidizing conditions during crystallization.

It is difficult to specify from which magmatic bodies (depth
 and size) the rock samples have been extracted, when they
 only consist of a set of xenoliths. The leucite lava was
 responsible for their extraction and we consider that leucite
 represents the last magma passing through the previous
 crystallized intrusions and dykes, being the residual magma
 coming from the crystallizing intrusions and lately injected
 towards the surface. The stability field of leucite in the
 presence of dissolved water is restricted when the pressure
 increases, leucite being finally removed beyond 0.8 GPa
 (Fudali 1963; Gittins et al. 1980 and references therein).
 The systematic occurrence of leucite in the xenoliths, even
 in pyroxenite, indicates that the xenoliths have crystallized
 under relatively low $P_{\text{H}_2\text{O}}$, not above the 0.3–0.8 GPa range,
 i.e., at a maximum depth of 25 km. This maximum depth
 corresponds to the xenoliths showing frequent and early
 crystallization of phlogopite (Prelević et al. 2015).

Calcite crystallization depends not only on the composition
 and evolution of the dissolved fluid phase in magma, but
 also on the low-temperature alteration processes. This is
 true for the calcite-bearing syenite xenoliths and for the
 kamafugite-type xenoliths. In the CO_2 vs CaO diagram
 (Appendix 3), CO_2 is higher in the kamafugite and syenite
 xenoliths than in the pyroxenite and leucitolite cumulates

825 (see Table 2). The kamafugite and syenite evolved liquids
 826 appear to be enriched in CO₂ relative to H₂O. Early phlogo-
 827 pite fractionation may have increased the CO₂/H₂O ratio in
 828 the dissolved fluid phase.

829 As explained by Yoder (1986) and McBirney (1984)
 830 for the Ultrapotassic Shonkin sag laccolith (Montana), it
 831 is difficult to explain the relationships between all types of
 832 rocks by a single fractional crystallization process from a
 833 single primary magma; in addition, Eğirdir xenoliths are
 834 not demonstrated to be all cogenetic. Other processes could
 835 also operate during the crystallization of intrusions: (i)
 836 percolation-reaction of the residual melt through the cumu-
 837 lates by infiltration metasomatism, as it is assumed in the
 838 mafic-ultramafic cumulates of layered intrusions near the
 839 solidus (Irvine 1980; Tait et al. 1984; Sparks et al. 1985;
 840 Brandeis and Jaupart 1986; Boudreau 1995); (ii) volatile
 841 transfer of Na relative to K explaining why the leucitolite
 842 cumulates are very depleted in Na₂O (McBirney 1984; Pec-
 843 cerillo 1994); (iii) mobile pneumatophile elements such as
 844 Th, during the hydrothermal activity at low pressure, and
 845 percolation of a CO₂-rich fluid phase exsolved from the
 846 residual magma.

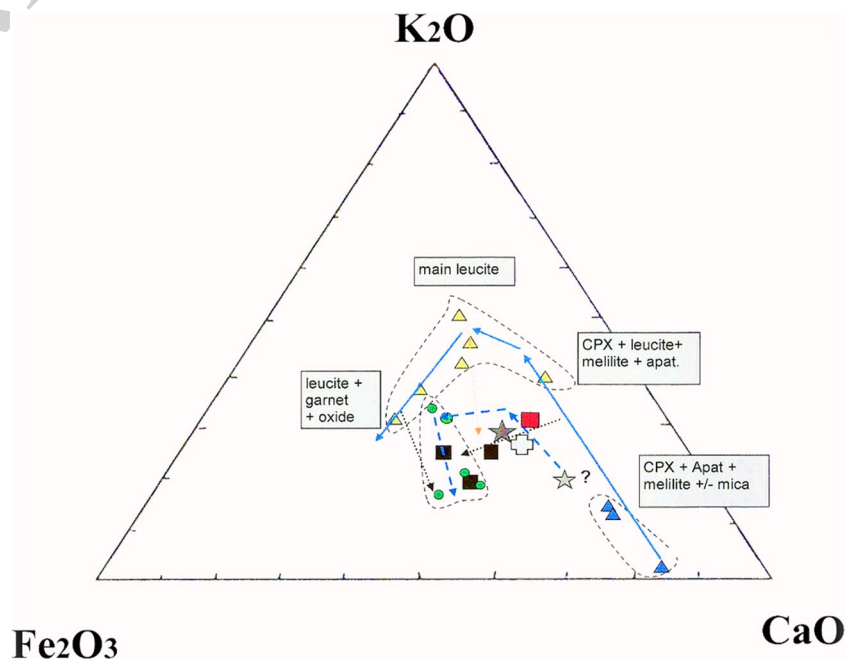
847 The evolution trends may be illustrated in the CaO/K₂O/
 848 Fe₂O₃ ternary diagram (Fig. 13). The primary melts are
 849 unknown. The less evolved KAM mafic magma assumed
 850 by Prelević et al. (2015) is close to the intermediate and
 851 salic ejecta found in the Alban Hill, Italy, especially the
 852 KLT kalsilitite xenolith (Lacroix 1893, 1917; Conticelli and
 853 Peccerillo 1992; Peccerillo 1992; Federico et al. 1994). The
 854 Eğirdir kamafugite seems to be more evolved and may be
 855 the result of efficient clinopyroxene and leucite fractionation,

856 leading to iron enrichment relative to CaO and K₂O, being
 857 thus related to the two main groups of Eğirdir cumulates
 858 (pyroxenite and leucitolite). The evolution represented by
 859 the leucitite lava is mainly controlled by leucite fractiona-
 860 tion, with iron content remaining globally constant, and is
 861 related to the crystallization of garnet and Fe-Ti oxides. The
 862 resulting liquid line of descent is questionable as not all
 863 xenoliths are cogenetic, especially the kamafugite-type and
 864 syenite xenoliths, which are most likely related to two dif-
 865 ferent magmas. If a reasonable liquid line of descent exists,
 866 it should be restricted from kamafugite to leucitite magmas
 867 in relation to the trend of assumed cumulates shown in this
 868 ternary diagram.

869 **Carbonatite xenolith significance and hypothetical**
 870 **origin**

871 The association of carbonatite and kamafugite magmas is
 872 known elsewhere in ultrapotassic magmatism, where blobs
 873 of calcio-carbonatite and kamafugite can be intimately asso-
 874 ciated. This relationships between two contrasted carbona-
 875 te-silicate conjugates have been described for example in
 876 magmatic rocks of the Mahlber complex, Germany (Solo-
 877 vova et al. 2003), in the West Qinling Province, China (Yu
 878 et al. 2003; Guo et al. 2014), in the Ruri Volcano, Kenya
 879 (Stoppa et al. 2003b), and in the Roman Province and
 880 Intra-mountain Ultra-alkaline Province, Italy (Stoppa and
 881 Wooley 1997; Stoppa et al. 2003a). In the Potassic Ultra-
 882 potassic Afyon volcanic Province, this intimate association
 883 has been observed in leucite-bearing phonolites (Elitok
 884 2019). This close association between carbonatite and very

Fig. 13 K₂O-Fe₂O₃-CaO ternary diagram. Blue triangle, pyroxenites; yellow triangle, leucitolites; black square, kamafugite type; red square, hyalophane-bearing syenite; small green dots, leucitites of Afyon ultrapotassic series (after Prelević et al. 2015); large green dot, leucitite of Egirdir. Green star, KAM assumed primary kamafugite magma (Prelević et al. 2015); white cross, KLT kalsilitolite xenolith from Alban Hills ejecta (Federico et al. 1994); gray star, hypothetical primary mafic magma. Blue arrows trend of successive cumulates; blue broken arrows, hypothetical magma evolution trend. The fractionation process would be governed by the mineral phases in the successive boxes



silica-undersaturated rocks has been attributed to an immiscibility process between carbonatite and silicate liquids. This immiscibility model between two silicate-carbonate conjugates has been experimentally tested at a relatively low pressure from <0.1 to 0.5 GPa (Koster van Groos and Wyllie 1966; Wyllie 1987; Kjarsgaard and Hamilton 1988; Lee and Wyllie 1998). Eğirdir xenoliths and their set of rock-forming minerals are plotted in the silica-alkali-carbonate diagram where the immiscibility fields are reported (Fig. 14) after Kjarsgaard and Hamilton (1988). The two arrows drawn from leucitolites and pyroxenites show that these cumulates can lead to the Eğırdir kamafugite through immiscibility in the 0.1–0.5-GPa pressure range. However, the theoretical conjugate carbonatitic liquid does not fit with the calcio-carbonatite xenolith found at Eğırdir: in this model, the composition of the Eğırdir carbonatite would require an additional process of accumulation of calcite and apatite crystals.

Another model for the genesis of the Eğırdir calcio-carbonatite would be to consider a direct interaction of the leucitic magma with the limestone basement (Elitok 2019).

Phreatomagmatic interaction with limestone basement or lacustrine carbonate during the explosive eruption could explain the calcitic matrix of the breccia occurring within the pipe and the peperite from the bottom of the Eğırdir phreatomagmatic deposit. However, stable isotope

compositions of calcite from the Eğırdir carbonatite indicate low crustal contamination. It seems that the origin of the Eğırdir carbonatite differs from the result of interaction between the leucitic magma with the limestone basement.

Globally, the composition of the Eğırdir calcio-carbonatite does not correspond to the intraplate carbonatite compositions related to HIMU and EM1 mantle components (Simonetti and Bell 1994; Woolley 2003; Tappe et al. 2003; Bell and Simonetti 2009) or to a direct CO₂-enriched fluid produced during the asthenosphere upwelling after the breakoff of the slab.

The composition of the Eğırdir carbonatite xenolith is more consistent with carbonatites found in an orogenic or post-orogenic geodynamical setting. The coexistence of ultrapotassic rocks and carbonatite has been a subject of debate for a long time (Foley 1992a, 1992b; Peccerillo 1984, 1998; Vollmer 1989; Peccerillo and Foley 1992; Ersoy et al. 2010; Prelević et al. 2008, 2010a, 2010b, 2012, 2015; Conticelli 1998; Conticelli et al. 2007, 2013, 2015). In a post-collisional geodynamical situation, the carbonatite mantle source would be phlogopite-bearing pyroxenite veins formed in a moderately depleted lithospheric mantle metasomatized by the fluid released by the sediments of the subducted slab. There is also a possibility to produce a carbonatitic melt by a fractionation-melting process of the metasomatized mantle source: this origin for carbonatite was proposed by Mitchell (2005). More extensive partial melting of the same source may product primary lamproite or kamafugite magmas, with high K/Na ratio, and high Ca, Mg, and CO₂ contents related to the metasomatized source. The differentiation process can also be at the origin of carbonatite: indeed, after extensive differentiation of melilitite and nephelinite magmas, a carbonatite residue may be produced (Mitchell 2005).

The mantle source of the UKAP magmatism and its complex metasomatization have been debated in the successive papers of Prelević et al. (2008, 2010a, b, 2012, 2015). Future isotopic studies of the Eğırdir xenoliths will be of great help to better understand the origin and relationships of these plutonic xenoliths with the Potassic Ultrapotassic Afyon volcanic Province, and to clarify whether they have fully or partially preserved their complex mantle geochemical signature, despite contamination processes during crustal magma injection and differentiation.

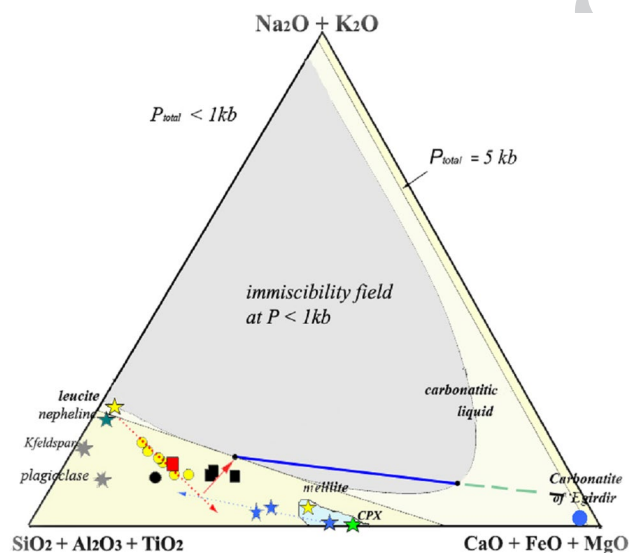


Fig. 14 Liquid immiscibility fields for $P_t < 0.1$ GPa and $P_t = 0.5$ GPa, in the $\text{SiO}_2 + \text{Al}_2\text{O}_3 + \text{TiO}_2 - \text{Na}_2\text{O} + \text{K}_2\text{O} - \text{CaO} + \text{FeO} + \text{MgO}$ ternary diagram. Blue stars, pyroxenite xenoliths; other stars, mineral phases. Black squares, kamafugite-type xenoliths; red square, hyalophane-bearing syenite; black dot, Eğırdir leucitite; yellow dot, leucitolite xenoliths. Blue straight line, conjugate silicate-carbonate liquids at $P < 0.1$ GPa. Green dashed line, conjugate liquids at 0.5 GPa (after Kjarsgaard and Hamilton 1988). Blue and red dotted lines with arrows, effect of leucite and clinopyroxene during fractional crystallization; the two trends cross at the average cumulate

Concluding remarks

The plutonic xenoliths found in the Eğırdir phreatomagmatic deposits have been extracted from dykes or/and plutonic intrusions related to batches of magma injected at crustal level.

Pyroxenite or leucitolite cumulates were formed during the differentiation of these crustal intrusions under a

960 maximum P_{total} of 0.8 GPa corresponding to a maximum
961 depth of 25 km. These rocks are assumed to be autoliths.

962 Eğirdir xenoliths are related to the strongly silica-depleted
963 ultrapotassic series of West Anatolia. Some of them have
964 kamafugite affinities and display the first occurrence of
965 kalsilite in this ultrapotassic series. Two forms of kalsilite
966 have been observed: a high-T hypersolvus homogeneous
967 form symptomatic of rapid cooling, and a subsolvus low-T
968 exsolved form associated with separate nepheline crystals
969 in slow-cooling intrusions. In syenite, feldspar crystallized
970 first as hyalophane, which played the same role of nepheline
971 during the leucite destabilization in K- and Ba-rich, and Na-
972 poor magmas.

973 The mineral paragenesis that controlled the fractional
974 crystallization process was mainly composed of clinopyrox-
975 ene apatite, melilite, phlogopite, and leucite, with additional
976 garnet and Fe-Ti oxides during the near-solidus evolution
977 of leucitolite cumulates. Phlogopite crystallization in some
978 pyroxenite indicates that partial $P_{\text{H}_2\text{O}}$ was high during their
979 crystallization, leading to an increase of the $\text{CO}_2/\text{H}_2\text{O}$ ratio
980 in the dissolved fluid phase.

981 The trace elements of the investigated xenoliths corre-
982 sponding to liquid compositions (kamafugite and syenite
983 types) indicate an orogenic/post-orogenic geodynamical
984 setting as assumed for the Potassic Ultrapotassic Afyon vol-
985 canic Province (Prelević et al. 2008, 2015) and the Roman
986 Province, Italy (Peccerillo 1990; Conticelli et al. 2013).

987 A carbonatite xenolith has been found for the first time in
988 this area. There are no convincing petrographic arguments to
989 support an immiscibility process between two silicate-car-
990 bonate conjugates. C and O stable isotopic compositions on
991 calcite indicate that the carbonatite has a mantle origin with
992 relatively limited crustal contamination. The origin of the
993 carbonatite by differentiation from a primitive kamafugite-
994 type magma, or by a fractionation-melting process of a meta-
995 somatized mantle source remains to be tested in the future.

996 New isotopic data on Eğirdir xenoliths, especially on
997 carbonatite- and kamafugite-type xenoliths, are needed to
998 better understand their origin, their possible cogenesis, and

999 **AQ14** mantle sources.

1000 **Supplementary Information** The online version contains supplemen-
1001 tary material available at <https://doi.org/10.1007/s12517-023-11766-7>.

1002 **Acknowledgements** Special thanks to E. Chassefière, past head of the
1003 GEOPS research team, N. Özgür, and F. Yağmurlu past dean of the
1004 Süleyman Demirel University. M. Fialin and N. Rividi are thanked
1005 for microprobe analysis assistance at Camparis Lab., Université
1006 Paris-Sorbonne, also V. Godard for the excellent polish fine sections.
1007 L. Weinberg is thanked to improve the English language. An anonym-
1008 ous reviewer is thanked for his comments on an earlier version of
1009 the manuscript. J.P. Liégeois is warmly thanked for careful review of
1010 the manuscript.

1011 **Funding** This work was financially supported by the UMR CNRS 8148
1012 GEOPS, Dpt. Sciences de la Terre, Université Paris-Saclay, and the

Süleyman Demirel University, Isparta, Turkey for field work support
and accommodations. 1013 1014

Declarations 1015

Conflict of interest The author(s) declare that they have no competing
interests. 1016 1017

References

- Akal C (2003) Mineralogy and geochemistry of melilite leucites, 1019
Balçıkhisar, Afyon (Turkey). *Turk J of Earth Sci* 12:215–239 1020
- Akal C, Helvacı C, Prelević D, van den Bogaard P (2013) High-K 1021
volcanism in the Afyon region, western Turkey: from Si- 1022
oversaturated to Si-undersaturated volcanism. *Int J Earth Sci* 1023
102:435–453 1024
- Alici P, Temel A, Gourgaud A, Kieffer G, Gündoğdu MN (1998) 1025
Petrology and geochemistry of potassic rocks in the Gölcük area 1026
(Isparta, SW Turkey): genesis of enriched alkaline magmas. *J* 1027
Volc Geoth Res 85(1–4):423–446 1028
- Aurisicchio C, Federico M (1985) Nepheline - kalsilite microper- 1029
thites in ejecta from the Alban Hills (Italy). *Bull Geol Soc Finl* 1030
57(1–2):129–137 1031
- Bailey K, Kearns S, Mergoil J, Mergoil-Daniel J, Paterson B (2006) 1032
Extensive dolomitic volcanism through the Limagne Basin, cen- 1033
tral France: a new form of a carbonatitic activity. *Mineral Mag* 1034
70:1–6 1035
- Beccaluva L, Di Girolamo P, Serri G (1991) Petrogenesis and tec- 1036
tonic setting of the Roman volcanic province. *Italy Lithos* 1037
26(3–4):191–221 1038
- Becker-Platen JD, Benda L, Steffens P (1977) Lith-Und biostratig- 1039
raphische Deutung radiometrischer altersbestimmungen aus 1040
dem Jungtertiär der Tuerkei (Känozoikum und Braunkohle der 1041
Turkei, 18). *Geol Jahrbuch* 25:139–167 1042
- Beccaluva L, Bianchini G, Wilson M (eds) (2012). Cenozoic volcan- 1043
ism in the Mediterranean Area. *Geol. Soc. Am. Spec. Paper* 418, 1044
171–202. 1045
- Bell K (2005) Carbonatites. In: Selley RC, Cocks LRM, Plimer IR (eds) 1046
Encyclopedia of Geology. Elsevier, Amsterdam, pp 217–233 1047
- Bell K, Powell JL (1969) Strontium isotopic studies of alkalic rocks: 1048
the potassium-rich lavas of the birunga and Toro—Ankole 1049
Regions, East and Central Equatorial Africa. *J Petrol* 10:536–572 1050
- Bell K, Simonetti A (2009) Source of parental melts to carbonatites- 1051
critical isotopic constraints. *Mineral Petrol* 98(1):77–89 1052
- Bell K, Tilton GR (2001) Nd, Pb and Sr isotopic compositions of East 1053
African carbonatites: evidence for mantle mixing and plume 1054
inhomogeneity. *J Petrol* 42:1927–1945 1055
- Bergman SC (1987). Lamproites and other potassium-rich igneous 1056
rocks : a review of their occurrence, mineralogy and geochemis- 1057
try. In Fitton JG., Upton BG (eds). *Alkaline igneous rocks*, *Geol.* 1058
Sci. Special Pub., 30, 103–190. 1059
- Bingöl E (1989). Geological map of Turkey (scale: 1/2.000.000), Gen- 1060
eral Directorate of Mineral Research and Exploration (MTA), 1061
Ankara, Turkey. 1062
- Boudreau AE (1995) Crystal aging and the formation of fine-scale 1063
layering. *Mineral Petrol* 1995(54):55–69 1064
- Brandeis G, Jaupart C (1986) On the interaction between convection 1065
and crystallization in cooling magma chambers. *Earth Planet* 1066
Sci Lett 77:345–361 1067
- Caran S (2016) Mineralogy and petrology of leucite ankaratrites with 1068
affinities to kamafugites and carbonatites from the Kayköy area, 1069
Isparta, SW Anatolia, Turkey: implications for the influences of 1070

- 1071 carbonatite metasomatism into the parental mantle sources of
1072 silica-undersaturated potassic magmas. *Lithos* 256–257:13–25
- 1073 Carmichael IS, Turner J, Verhoogen J (1974). *Igneous petrology*.
1074 McGraw-Hill, 739.
- 1075 Çoban H, Topuz G, Roden MF, Hoang N, Schwarz WH (2019) ⁴⁰Ar-
1076 ³⁹Ar dating and petrology of monzonite ejecta in tephra from
1077 Quaternary Gölcük volcano (Isparta, SW Turkey): tear-related
1078 contrasting metasomatic symptoms in extensional mantle-derived
1079 magmas. *Lithos* 330–331:160–176
- 1080 Chazot G, Mergoïl-Daniel J (2012) Co-eruption of carbonate and sili-
1081 cate magmas during volcanism in the Limagne graben, French
1082 Massif Central. *Lithos* 154:130–146
- 1083 Conticelli S, Peccerillo A (1992). Petrology and geochemistry of potas-
1084 satic and ultrapotassic volcanism in Central Italy: petrogenesis and
1085 inferences on the evolution of the mantle sources. In: Peccerillo
1086 A, Foley S (eds): Potassic and ultrapotassic magmas and their
1087 origin. *Lithos* 28, 221–240.
- 1088 Conticelli S (1998) The effect of crustal contamination on ultrapotassic
1089 magmas with lamproitic affinity: Mineralogical, geochemical and
1090 isotope data from the Torre Alfina lavas and xenoliths, Central
1091 Italy. *Chem Geol* 149:51–81
- 1092 Conticelli S, Carlson RW, Widom E, Serri G (2007) Chemical and
1093 isotopic composition (Os, Pb, Nd, and Sr) of Neogene to Quater-
1094 nary calc-alkalic, shoshonitic and ultrapotassic mafic rocks from
1095 the Italian Peninsula: inferences on the nature of their mantle
1096 sources. *Spec Paper Geol Soc Am* 418:171–202
- 1097 Conticelli S, Avanzinelli R, Poli G, Braschi E, Giordano G (2013) Shift
1098 from lamproite-like to leucititic rocks: Sr-Nd-Pb isotope data
1099 from the Monte Cimino volcanic complex vs. the Vico strato-
1100 volcano. *Central Italy Chem Geol* 353:246–266
- 1101 Conticelli S, Avanzinelli R, Ammannati E, Casalini M (2015) The
1102 role of carbon from recycled sediments in the shift from lam-
1103 proite to leucite in the Central Mediterranean region. *Lithos*
1104 232:174–196
- 1105 Cundari A (1979) Petrogenesis of leucite-bearing lavas in the Roman
1106 volcanic region, Italy. *Sabatini Lavas Contrib Mineral Petrol*
1107 70:9–21
- 1108 Di Battistini G, Montanini A, Vernia L, Venturelli G, Tonarini S (2001)
1109 Petrology of melilite-bearing rocks from the Montefiascone vol-
1110 canic complex (Roman Magmatic Province): new insights into
1111 the ultrapotassic volcanism of Central Italy. *Lithos* 59(1–2):1–24
- 1112 Doroshkevich AG, Ripp GS, Moore KR (2010) Genesis of the Khaluta
1113 alkaline-basic Ba-Sr carbonatite complex (West Transbaikala,
1114 Russia). *Miner Petrol* 98:245–268
- 1115 Edgar AD (1992) Barium-rich phlogopite and biotite from some Qua-
1116 ternary alkali mafic lavas, West Eifel, Germany *Eur J Mineral*
1117 4:321–330
- 1118 Edgar AD, Arima M (1981) Geochemistry of three potassium-rich
1119 ultrabasic lavas from the west branch of the African rift: infer-
1120 ences on their genesis. *Neues Jb Mineral Monatsh* 12:539–552
- 1121 Elitok Ö (2019) Geology and petrology of the potassic and ultrapotas-
1122 satic rocks from the northern part of Senirkent (Isparta-SW Tur-
1123 key): evidence of magma-carbonate wall-rock interactions. *Arab*
1124 *J Geosci* 12:1–23
- 1125 Erişen B (1972). Afyon-Heybeli (Kızılkilise) jeotermal araştırma
1126 sahasının jeolojisi ve jeotermal olanakları. *Maden Tetkik Arama*
1127 *Enstitüsü Raporu*, No:3107, (unpublished), Ankara, Türkiye.
- 1128 Ersoy EY, Helvacı C, Palmer MR (2010) Mantle source characteristics
1129 and melting models for the early-middle Miocene mafic volcan-
1130 ism in Western Anatolia: implications for enrichment processes
1131 of mantle lithosphere and origin of K-rich volcanism in post-
1132 collisional settings. *J Volc Geotherm Res* 198:112–128
- 1133 Essene EJ, Clafin CL, Giorgetti G, Mata PM, Peacor DR, Arkai P,
1134 Rathmell MA (2005) Two-, three- and four-feldspar assemblages
1135 with hyalophane and celsian: implications for phase equilibria
in BaAl₂Si₂O₈-CaAl₂Si₂O₈-NaAlSi₃O₈-KAlSi₃O₈. *Eur J Mineral* 17:515–535
- Federico M, Peccerillo A, Barbieri M, Wu TW (1994) Mineralogical
and geochemical study of granular xenoliths from the Alban Hills
volcano, Central Italy: bearing on the evolutionary processes in
potassic magma chambers. *Contrib Mineral Petrol* 115:384–401
- Ferguson AK, Cundari A (1982) Feldspar crystallization trends in
leucite-bearing and related assemblages. *Contrib Mineral Petrol*
81:212–218
- Foley SF, Venturelli G, Green DH, Toscani L (1987) The ultrapotassic
rocks: characteristics, classification and constraints for petroge-
netic models. *Earth Sci Rev* 24:81–134
- Foley S (1992a) Petrological characterization of the source components
of potassic magmas: geochemical and experimental constraints.
Lithos 28:187–203
- Foley S (1992b) Vein-plus-wall-rock melting mechanisms in the
lithosphere and the origin of potassic alkaline magmas. *Lithos*
28:435–453
- Fudali RF (1963) Experimental studies bearing on the origin of pseu-
doleucite and associated problems of alkalic rock systems. *Geol*
Soc Am Bull 74(109):1101–1126
- Gaeta M, Freda C, Christensen JN, Dallai L, Marra F, Karner DB,
Scarlato P (2006) Time-dependent geochemistry of clinopyrox-
ene from the Alban Hills (Central Italy): clues to the source and
evolution of ultrapotassic magmas. *Lithos* 86:330–346
- Gaspar JC, Wyllie PJ (1982) Barium phlogopite from the Jacupiranga
carbonatite. *Brazil Am Mineral* 67:997–1000
- Gittins J, Fawcett JJ, Brooks CK, Rucklidge JC (1980) Intergrowths of
nepheline-potassium feldspar and kalsilite-potassium feldspar: a
re-examination of the pseudo-leucite problem. *Contrib Mineral*
Petrol 73:119–126
- Guillou H, Scao V, Nomade S, Platevoet B, Blamart D (2017) De la
justesse des âges K-Ar : exemple de la datation de deux dômes
trachytiques du Gölcük (Turquie). *Quaternaire* 28(2):141–148
- Gupta AK, Chattopadhyay S, Chattopadhyay B, Arima M (2006)
Experimental Study of the system diopside-nepheline-sanidine
at 0.1, 1 and 2 GPa [P_(H₂O)=P_(Total)]: its significance in the ge-
nesis of alkali-rich basic and ultrabasic rocks. *Lithos* 86:91–109
- Gupta AK, Yagi K (1980). Petrology and genesis of leucite-bear-
ing rocks, Springer-Verlag, 252.
- Gupta AK (2015). Origin of potassium-rich silica-deficient igneous
rocks. Springer-Verlag, 450.
- Guo P, Niu Y, Yu X (2014) A synthesis and new perspective on the
petrogenesis of kamafugites from West Qinling, China, in the
global context. *J Asian Earth Sc* 79:86–96
- Gürsu S, Gönçüoğlu MC, Bayhan H (2004) Geology and geochemistry
of the Pre-early Cambrian rocks in the Sandıklı Area: implica-
tions for the Pan-African evolution of NW Gondwanaland. *Gond-
wana Res* 7(4):923–935
- Holness MB, Vernon RH (2014). The influence of interfacial energies
on igneous microstructures. In: Charlier BLA, Namur O, Latypov
RM, Tegner C (eds). *Layered intrusions*. Dordrecht Springer,
183–228.
- Holness MB, Vukmanovic Z, Mariani E (2017) Assessing the role of
compaction in the formation of adcumulates: a microstructural
perspective. *J Petrol* 58:643–674
- Holness MB, Clemens JD, Vernon RH (2018) How deceptive are
microstructures in granitic rocks? Answers from integrated phys-
ical theory, phase equilibrium, and direct observations. *Contrib*
Mineral Petrol 173(8):2–18
- İnal A (1975) Afyon bölgesi gölsel Neojen’inde bulunmuş yeni iki
Gastropod türü ve bir alt tanımı. *Türkiye Jeoloji Kurumu Bülteni*
18(2):161–164
- Veksler IV, Fedorchuk YM, Nielsen TFD (1998) Phase equilibria in the
silica-undersaturated part of the KAlSiO₄ – Mg₂SiO₄ – Ca₂SiO₄

- 1201 – SiO₂ – F system at 1 atm and the larnite-normative trend of
1202 melt evolution. *Contrib Mineral Petrol* 151:347–363
- 1203 Irvine TN (1980) Magmatic infiltration metasomatism, double-dif-
1204 fusive fractional crystallization and adcumulus growth in the
1205 Muskox and other layered intrusions. In: Hargraves RB (ed)
1206 *Physics of magmatic processes*. Princeton University Press,
1207 Princeton, pp 325–383
- 1208 Kampunzu AB, Lubala RT (1991). *Magmatism in extensional struc-*
1209 *tural settings: the Phanerozoic African Plate*. Springer, 637.
- 1210 Koçyiğit A (1984a) Güneybatı Türkiye ve yakın dolayında levha içi
1211 yeni tektonik gelişim. *Türkiye Jeoloji Bülteni* 27:1–16
- 1212 Koçyiğit A (1984b). Tectono-stratigraphic characteristics of Hoyran
1213 Lake region (Isparta Bend). In: Tekeli O, Göncüoğlu MC (eds).
1214 *Geology of the Taurus Belt. Proceedings of the International*
1215 *Symposium held by the Mineral Research and Exploration Insti-*
1216 *tute, 26–29 September 1983, 53–67, Ankara, Turkey.*
- 1217 Keller J (1983) Potassic lavas in the orogenic volcanism of the Mediter-
1218 ranean area. *J Volc Geotherm Res* 18:321–335
- 1219 Lacroix A (1893) Les enclaves des roches volcaniques. *Mâcon Protal*
1220 *1(8):770*
- 1221 Lacroix A (1917) Les roches grenues d'un magma leucitique étudiées
1222 à l'aide des blocs holocristallins de la Somma. *C R Acad Sc*
1223 *Paris* 165:481–487
- 1224 Laporte D, Provost A (2000) Equilibrium geometry of a fluid phase in
1225 a polycrystalline aggregate with anisotropic surface energies: dry
1226 grain boundaries. *J Geophys Res* 105:25937–25953
- 1227 Larsen LM (1976) Clinopyroxenes and coexisting mafic minerals
1228 from the alkaline Ilimaussaq intrusion, South Greenland. *J Pet-*
1229 *rol* 12:303–315
- 1230 Laval M, Hottin AM (1992) The Mlindi ring structure. An example
1231 of an ultrapotassic pyroxenite to syenite differentiated complex.
1232 *Geol Rundschau* 81:737–757
- 1233 Lee WJ, Wyllie PJ (1998) Processes of crustal carbonatite formation
1234 by liquid immiscibility and differentiation, elucidated by model
1235 systems. *J Petrol* 39:2005–2013
- 1236 Lefèvre C, Bellon H, Poisson A (1983) Occurrence of leucitites among
1237 the Pliocene volcanics of Isparta (Western Taurides, Turkey). *C*
1238 *R Acad Sci II* 297:367–372
- 1239 Le Maitre RW (2002) *Igneous rocks, a classification and glossary of*
1240 *terms, 2nd edn*. Cambridge Univ. Press, p 236
- 1241 Mansker WL, Ewing RC, Keil K (1979) Barian-titanian biotites in
1242 nephelinites from Oahu. *Hawaii Am Mineralogist* 64:156–159
- 1243 Marsh BD (1998) On the interpretation of crystal size distributions in
1244 magmatic systems. *J Petrol* 39:553–599
- 1245 Marsh BD (2007) Crystallization of silicate magmas deciphered using
1246 crystal size distributions. *J Am Ceram Soc* 90:746–757
- 1247 McBirney AR (1984). *Igneous petrology*. Freeman, Cooper and Co.
1248 eds. 504.
- 1249 McBirney AR (2007) Constitutional zone refining of layered intrusions.
1250 In: Parsons I (ed) *Origins of igneous layering*. Reidel, Boston,
1251 pp 437–452
- 1252 McBirney AR (2009) Factors governing the textural development of
1253 Skaergaard gabbros. *Lithos* 111:1–5
- 1254 McBirney AR, Boudreau AE, Marsh B (2009) Comments on “Tex-
1255 tural maturity of cumulates: a record of chamber filling, liqui-
1256 dous assemblage, cooling rate and large-scale convection in mafic
1257 layered intrusions” and “a textural record of solidification and
1258 cooling in the Skaergaard Intrusion, East Greenland.” *J Petrol*
1259 *50:93–95*
- 1260 Mitchell RH (2005) Carbonatites and carbonatites and carbonatites.
1261 *Can Mineral* 43:2049–2068
- 1262 Mitchell RH, Bell K (1976) Rare earth element geochemistry of potas-
1263 sic lavas from the Birunga and Toro-Ankole regions of Uganda.
1264 *Africa Contrib Mineral Petrol* 58:293–303
- 1265 Mitchell RH, Bergman SC (1991) *Petrology of lamproites*. Plenum
1266 Press, New York, p 456
- Mitchell RH, Platt RG (1978) Mafic mineralogy of ferroaugite syen-
ite from the Coldwell alkaline complex, Ontario. *Canada J*
Petrol 19(4):627–651
- Mitchell RH, Platt RG (1982) Mineralogy and petrology of nepheline
syenites from the Coldwell alkaline complex, Ontario. *Canada*
J Petrol 23:186–214
- Mitchell RH, Vladykin NV (1996) Compositional variation of pyrox-
ene and mica from the Little Murun ultrapotassic complex,
Aldan Shield. *Russia Min Mag* 60(403):907–925
- Okay AI (2011) Tavşanlı Zone: The northern subducted margin
of the Anatolide-Tauride block. *Bullet Mineral Res Explor*
142:191–221
- Peccherillo A, Poli G, Tolomeo L (1984) Genesis, evolution and tectonic
significance of K-rich volcanics from the Alban Hills
(Roman comagmatic region) as inferred from trace element
geochemistry. *Contrib Mineral Petrol* 86:230–240
- Peccherillo A (1990) On the origin of the Italian potassic magmas -
comments. *Chem Geol* 85(1–2):183–191
- Peccherillo A (1992) Potassic and ultrapotassic rocks: compositional
characteristics, petrogenesis, and geologic significance. *Epi-*
sodes 15(4):243–251
- Peccherillo A (1994) Mafic ultrapotassic magmas in Central Italy :
geochemical and petrological evidence against primary mag-
mas. *Miner Petrogr Acta V(XXXVII):229–245*
- Peccherillo A, Foley S (eds) (1992). Potassic and ultrapotassic mag-
mas and their origin. *Lithos*, 28, 3-6, 453.
- Perini G, Conticelli S (2002) Crystallization conditions of leucite-
bearing magmas and their implications on the magmatological
evolution of ultrapotassic magmas: the Vico Volcano, Central
Italy. *Miner Petrol* 74:253–276
- Platevoet B, Elitok Ö, Guillou H, Bardintzeff JM, Yağmurlu F,
Nomade S, Poisson A, Deniel C, Özgür N (2014) Petrology of
Quaternary volcanic rocks and related plutonic xenoliths from
Gölcük volcano, Isparta Angle, Turkey: Origin and evolution
of the high-K alkaline series. *J Asian Earth Sc* 92:53–76
- Poucllet A (1980) Contribution à la systématique des laves alcalines,
les laves du rift de l'Afrique Centrale (Zaire-Uganda). *Bull*
Volcanol 43(3):527–540
- Prelević D, Foley SF, Romer RL, Cvetković V, Downes H (2005)
Tertiary ultrapotassic volcanism in Serbia: constraints on
petrogenesis and mantle source characteristics. *J Petrol*
46:1443–1487
- Prelević D, Foley SF, Romer RL, Conticelli S (2008) Mediterra-
nean Tertiary lamproites derived from multiple source com-
ponents in postcollisional geodynamics. *Geoch Cosmoch Acta*
72:2125–2156
- Prelević D, Akal C, Romer RL, Foley SF (2010a) Lamproites as indi-
cators of accretion and/or shallow subduction in the assembly
of South-western Anatolia. Turkey, *Terra Nova* 22(6):443–452
- Prelević D, Foley SF, Stracke A, Romer RL, Conticelli S (2010b) Hf
isotope compositions of Mediterranean lamproites: mixing of
melts from asthenosphere and crustally contaminated mantle
lithosphere. *Lithos* 119:297–312
- Prelević D, Akal C, Foley SF, Romer RL, Stracke A, van den Bogaard
L (2012) Ultrapotassic mafic rocks as geochemical proxies for
postcollisional mantle dynamics of lithosphere: the case of SW.
Anatolia-Turkey *J Petrol* 53:1019–1105
- Prelević D, Akal C, Romer RL, Mertz-Kraus R, Helvacı C (2015) Mag-
matic response to slab tearing: constraints from the Afyon Alka-
line Volcanic Complex, Western Turkey. *J Petrol* 56(3):527–562
- Ridolfi F, Renzulli A, Macdonald R, Upton B G J (2006) Peralkaline
syenite autoliths from Kilombe volcano, Kenya Rift Valley: evi-
dence for subvolcanic interaction with carbonatitic fluids. *Lithos*
91:373–392
- Sahama TG (1974) Potassium rich-rocks. In: Sorensen H (ed) *Alkaline*
rocks. Wiley, London, U.K., pp 96–109

1333 Savaşçin MY, Birsoy R, Dag N, Nohutçu E (1994) Kirka-Afyon-Isparta
1334 structural trend and Alkaline rock associations (Anatolia). Bull
1335 Geol Soc Greece VXXX(3):89–98
1336 Savaşçin MY, Oyman T (1998) Tectonomagmatic evolution of alkaline
1337 volcanics at the Kirka-Afyon-Isparta structural trend. SW Turkey
1338 Turk J Earth Sci 7:201–214
1339 Schönerberger J, Marks M, Wagner T, Markl G (2006) Fluid-rock
1340 interaction in autoliths of agpaitic nepheline syenites in the Ilf-
1341 maussağ intrusion, South Greenland. Lithos 91:331–351
1342 Seifert W, Kämpf H (1994) Ba-enrichment in phlogopite of a nephelin-
1343 ite from Bohemia. Eur J Mineral 6:497–502
1344 Simonetti A, Bell K (1994) Nd, Pb and Sr isotopic data from the Napak
1345 carbonatite-nephelinite centre, eastern Uganda: an example
1346 of open-system crystal fractionation. Contrib Mineral Petrol
1347 115:356–366
1348 Sparks RSJ, Huppert HE, Kerr RC, McKenzie DP, Tait SR (1985) Post-
1349 cumulus processes in layered intrusions. Geol Mag 122:555–568
1350 Solovova IP, Girmis AV, Rass IT, Keller J, Kononkova NN (2003) Dif-
1351 ferent styles of evolution of CO₂-rich alkaline magmas: the role
1352 of melt composition in carbonate-silicate liquid immiscibility.
1353 Per Mineral Eurocarb Workshop Spec Issue 1(LXXII):87–93
1354 Stoppa F (2003) Consensus and open questions about Italian
1355 CO₂-driven magma from the mantle. Per Mineral Eurocarb
1356 Workshop Special Issue 1(LXXII):1–8
1357 Stoppa F, Cundari A, Rosatelli G, Wooley AR (2003) Leucite melilito-
1358 lites in Italy: genetic aspects and relationships with associated
1359 alkaline rocks and carbonatites. Per Mineral Eurocarb Workshop
1360 Special Issue 1(LXXII):223–251
1361 Stoppa F, Rosatelli G, Wall F, Le Bas MJ (2003) Texture and mineral-
1362 ogy of tuffs and tuffisites at Ruri volcano in western Kenya: a
1363 carbonatite, melilite, mantle-debris trio. Per Mineral Eurocarb
1364 Workshop Special Issue 1(LXXI):181–204
1365 Stoppa F, Loyd EL, Rosatelli G (2003) CO₂ as the propellant of
1366 carbonatite-kamafugite cognate pairs and the eruption of dia-
1367 tremic tuffisite. Per Mineral Eurocarb Workshop Special Issue
1368 1(LXXII):205–222
1369 Sun SS, McDonough W (1989) Chemical and isotopic systematics of
1370 oceanic basalts: implications for mantle composition and pro-
1371 cesses In: Saunders AD, Norry MJ (eds) Magmatism in the
1372 oceanic basins. Geol Soc London Spec Publ 42(1):313–345
1373 Tait SR, Huppert HE, Sparks RSJ (1984) The role of composi-
1374 tional convection in the formation of adcumulate rocks. Lithos
1375 17:139–146

Tappe S, Foley SF, Pearson DG (2003) The kamafugites of Uganda: a
1376 mineralogical and geochemical comparison with their Italian and
1377 Brazilian analogues. Per Mineral Eurocarb Workshop Special
1378 Issue 1(LXXII):51–77
1379 Tuttle OF, Smith JV (1958) The nepheline-kalsilite system; II, Phase
1380 relations. Amer J Sci 256:571–589
1381 Thornton CP, Tuttle OF (1960) Chemistry of igneous rocks. I: the dif-
1382 ferentiation index. Amer J Sci 258:664–684
1383 Vollmer R (1989) On the origin of the Italian potassic magmas: 1.
1384 Discus Contrib Chem Geol 74(3–4):229–239
1385 Wagner C, Velde D (1986) The mineralogy of K-richterite-bearing
1386 lamproites. Am Mineral 71:17–37
1387 Wagner C, Velde D, Mokhtari A (1987) Sector zoned phlogopites in
1388 igneous rocks. Contrib Mineral Petrol 96:186–191
1389 Woolley AR (2003) Igneous silicate rocks associated with carbonatites:
1390 their diversity, relative abundances and implications for carbon-
1391 atite genesis. Per Mineral Eurocarb Workshop Special Issue
1392 1(LXXII):9–17
1393 Woolley AR, Bergman SC, Edgar AD, Le Bas MJ, Mitchell RH, Rock
1394 NMS, Scott-Smith BH (1996) Classification of lamprophyres,
1395 lamproites, kimberlites, and the kalsilitic, melilitic, and leucitic
1396 rocks. Can Mineral 34:175–186
1397 Xuehu Y, Zhidan Z, Xuanxue M, Shangguo S, Deqin Z, Yonglei W
1398 (2003) The petrological and mineralogical characteristics of
1399 Cenozoic kamafugite and carbonatite association in West Qin-
1400 ling, Gansu Province, China. Per Mineral Eurocarb Workshop
1401 Special Issue 1(LXXII):261–179
1402 Yağmurcu F, Savaşçin MY, Ergün M (1997) Relation of the alkaline
1403 volcanism and active tectonism within the evolution of the
1404 Isparta angle, SW Turkey. J Geol V105:717–728
1405 Yoder HS (1986) Potassium-rich rocks: phase analysis and heteromor-
1406 phic relations. J Petrol 27(5):1215–1228
1407 Zeng RS, MacKenzie WS (1984) Preliminary report on the system
1408 NaAlSi₃O₈-KAlSi₃O₈-SiO₂-H₂O at P_{H₂O} = 5 kbar. Bull Minéral
1409 107:571–577
1410

Springer Nature or its licensor (e.g. a society or other partner) holds
1411 exclusive rights to this article under a publishing agreement with the
1412 author(s) or other rightsholder(s); author self-archiving of the accepted
1413 manuscript version of this article is solely governed by the terms of
1414 such publishing agreement and applicable law.
1415